

RESEARCH

Open Access



Photogenerated reactive oxygen species and hyperthermia by Cu₃SnS₄ nanoflakes for advanced photocatalytic and photothermal antibacterial therapy

Yangzi Yang^{1,2}, Chengwei Wang^{1,2}, Ning Wang^{1,2}, Jiaxin Li^{2,3}, Yingchun Zhu⁵, Jiantao Zai^{4*}, Jingke Fu^{1,2*} and Yongqiang Hao^{1,2*} 

Abstract

Background: The rapid spread of infectious bacteria has brought great challenges to public health. It is imperative to explore effective and environment-friendly antibacterial modality to defeat antibiotic-resistant bacteria with high biosafety and broad-spectrum antibacterial property.

Results: Herein, biocompatible Cu₃SnS₄ nanoflakes (NFs) were prepared by a facile and low-cost fabrication procedure. These Cu₃SnS₄ NFs could be activated by visible light, leading to visible light-mediated photocatalytic generation of a myriad of reactive oxygen species (ROS). Besides, the plasmonic Cu₃SnS₄ NFs exhibit strong near infrared (NIR) absorption and a high photothermal conversion efficiency of 55.7%. The ROS mediated cellular oxidative damage and the NIR mediated photothermal disruption of bacterial membranes collaboratively contributed to the advanced antibacterial therapy, which has been validated by the efficient eradication of both Gram-negative *Escherichia coli* and Gram-positive methicillin-resistant *Staphylococcus aureus* strains in vitro and in vivo. Meanwhile, the exogenous copper ions metabolism from the Cu₃SnS₄ NFs facilitated the endothelial cell angiogenesis and collagen deposition, thus expediting the wound healing. Importantly, the inherent localized surface plasmon resonance effect of Cu₃SnS₄ NFs empowered them as an active substrate for surface-enhanced Raman scattering (SERS) imaging and SERS-labeled bacteria detection.

Conclusions: The low cost and biocompatibility together with the solar-driven broad-spectrum photocatalytic/photothermal antibacterial property of Cu₃SnS₄ NFs make them a candidate for sensitive bacteria detection and effective antibacterial treatment.

Keywords: Reactive oxygen species, Cu₃SnS₄, Photocatalytic, Photothermal, Antibacterial therapy

*Correspondence: zaijiantao@sjtu.edu.cn; fujingke@sjtu.edu.cn;
hyq_ghospital@hotmail.com

¹ Shanghai Key Laboratory of Orthopaedic Implant, Department of Orthopaedic Surgery, Shanghai Ninth People's Hospital, Shanghai Jiao Tong University School of Medicine, Shanghai 200011, China

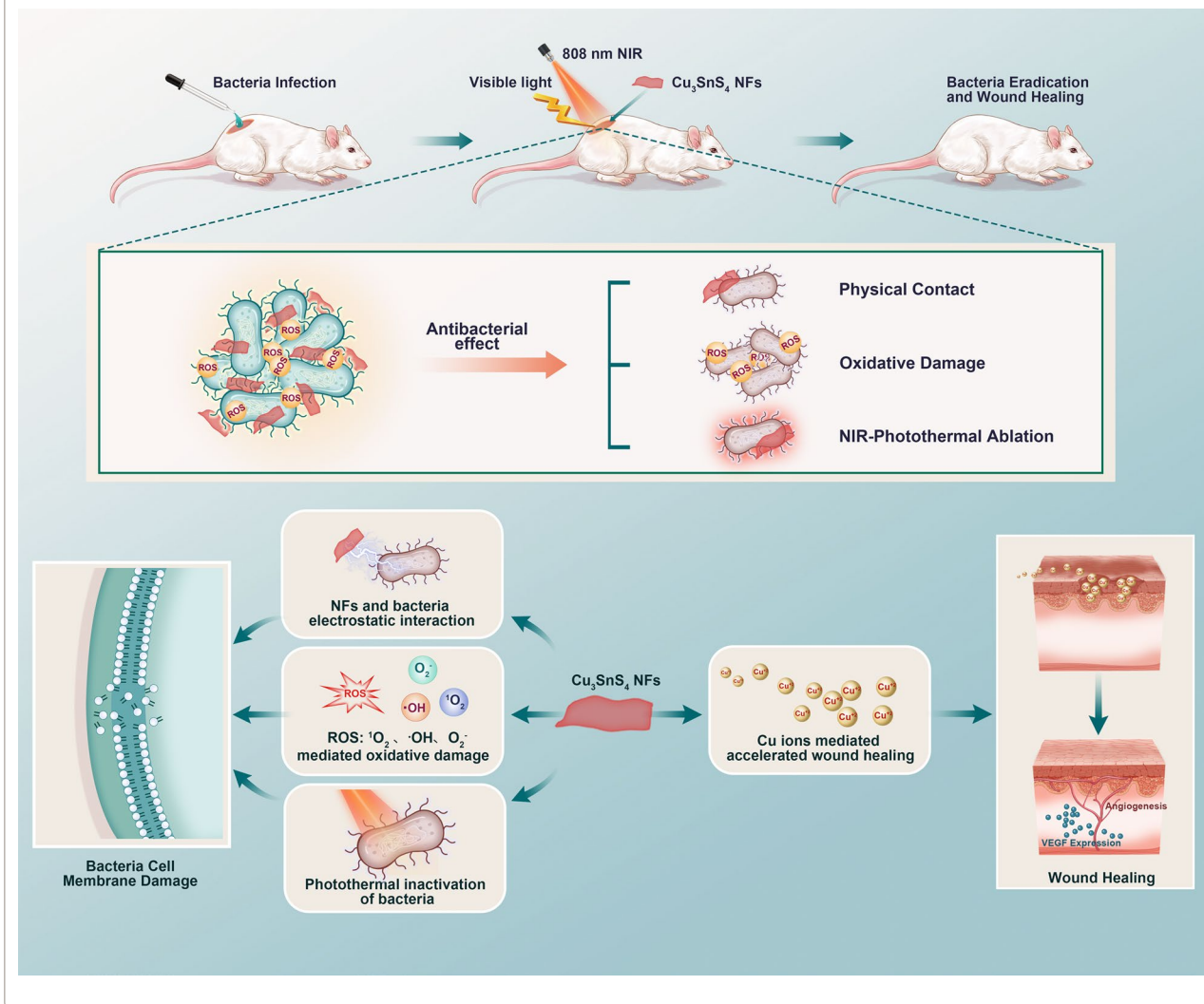
⁴ Shanghai Electrochemical Energy Devices Research Center, School of Chemistry and Chemical Engineering and State Key Laboratory of Metal Matrix Composites, Shanghai Jiao Tong University, Shanghai 200240, China

Full list of author information is available at the end of the article



© The Author(s) 2022. **Open Access** This article is licensed under a Creative Commons Attribution 4.0 International License, which permits use, sharing, adaptation, distribution and reproduction in any medium or format, as long as you give appropriate credit to the original author(s) and the source, provide a link to the Creative Commons licence, and indicate if changes were made. The images or other third party material in this article are included in the article's Creative Commons licence, unless indicated otherwise in a credit line to the material. If material is not included in the article's Creative Commons licence and your intended use is not permitted by statutory regulation or exceeds the permitted use, you will need to obtain permission directly from the copyright holder. To view a copy of this licence, visit <http://creativecommons.org/licenses/by/4.0/>. The Creative Commons Public Domain Dedication waiver (<http://creativecommons.org/publicdomain/zero/1.0/>) applies to the data made available in this article, unless otherwise stated in a credit line to the data.

Graphical Abstract



Background

The continuous and rapid spread of infectious bacteria has brought great challenges to public health. This challenge has been further exacerbated by the excessive use of antibiotics, which cultivates multidrug-resistant “super-bacteria” that may go out of the control of traditional antibiotics treatment [1]. During the past few years, a series of antibacterial materials, such as peptides, polymers, quaternary ammonium salts, metal oxides, and inorganic nanoparticles [2–6], have proven as bactericidal or bacteriostatic agents due to their unique antibacterial mechanisms. Although the great potential of the abovementioned antibacterial materials as alternative antibiotics, further clinical applications are limited by their potential biotoxicity and low antibacterial

efficiency. It is imperative to explore more effective and environment-friendly antibacterial modality to defeat antibiotic-resistant bacteria with high biosafety and broad-spectrum antibacterial property.

Recently, photocatalytic technology has emerged as a promising option for administrating antibiotic-resistant bacteria in water disinfection [7–10]. Photocatalysis involves the use of solar light for activating photocatalysts to split water, followed by the generation of a myriad of reactive oxygen species (ROS) such as hydrogen peroxide (H_2O_2), hydroxyl radicals ($\cdot\text{OH}$), superoxide radicals ($\text{O}_2^{\cdot-}$) and singlet oxygen (${}^1\text{O}_2$) [11–15]. These ROS could react with proteins, lipids, polysaccharides as well as other constituents of bacteria, leading to oxidative damage of bacterial membrane and ultimate cell death

[13, 16–18]. It is noteworthy that ROS-based photocatalysis has been revealed to play a vital role in preventing bacterial biofilms formation, showing great potential for even antibiotic-resistant bacteria [19, 20]. The ideal properties for photocatalysts in antibacterial therapy are (i) facile and low-cost fabrication procedure for future mass application; (ii) environment-friendly and high biosafety to normal tissues; (iii) efficient photocatalytic reactivity with extended absorption region to achieve full spectrum solar-driven photocatalysis; (iv) broad-spectrum antibacterial property for even multidrug-resistant bacteria. Ternary Cu₃SnS₄ is a p-type semiconductor with a high absorption coefficient ($\sim 10^5 \text{ cm}^{-1}$) and a tunable optical band gap (0.8–1.7 eV) [21]. The narrow band gap of Cu₃SnS₄ enables it an extended absorption in visible and near infrared (NIR) regions. Since semiconductor photocatalysts such as ZnO, TiO₂ and Ag-C₃N₄ composite [22] commonly are only active in the ultraviolet (UV) light spectrum, which occupies only 4% of the solar spectrum [7]. The higher and extended optional absorption of Cu₃SnS₄ in the visible region (occupies 44% of the solar spectrum) thus makes it a desired photocatalyst for visible (Vis) light activatable antibacterial applications. More importantly, the plasmonic Cu₃SnS₄ exhibits strong NIR absorption and high quantum efficiency, which could be converted to thermal energy and induce NIR based photothermal sterilization [23–26]. Notably, unlike the narrow bandgap metal sulfides such as CdS, PbS, ZnInS₄, AgGaS₂ and ZnCdS, which suffer from drawbacks of elemental toxicity (Cd and Pb) and higher costs (In and Ga). The Cu₃SnS₄ is consisted of low-cost and non-toxic elements of Cu, Sn and S, which have been reported to play a vital role in regulating the metabolic activity in skin pigmentation, tissue repairs, and acting as building blocks of proteins and tissues [27, 28].

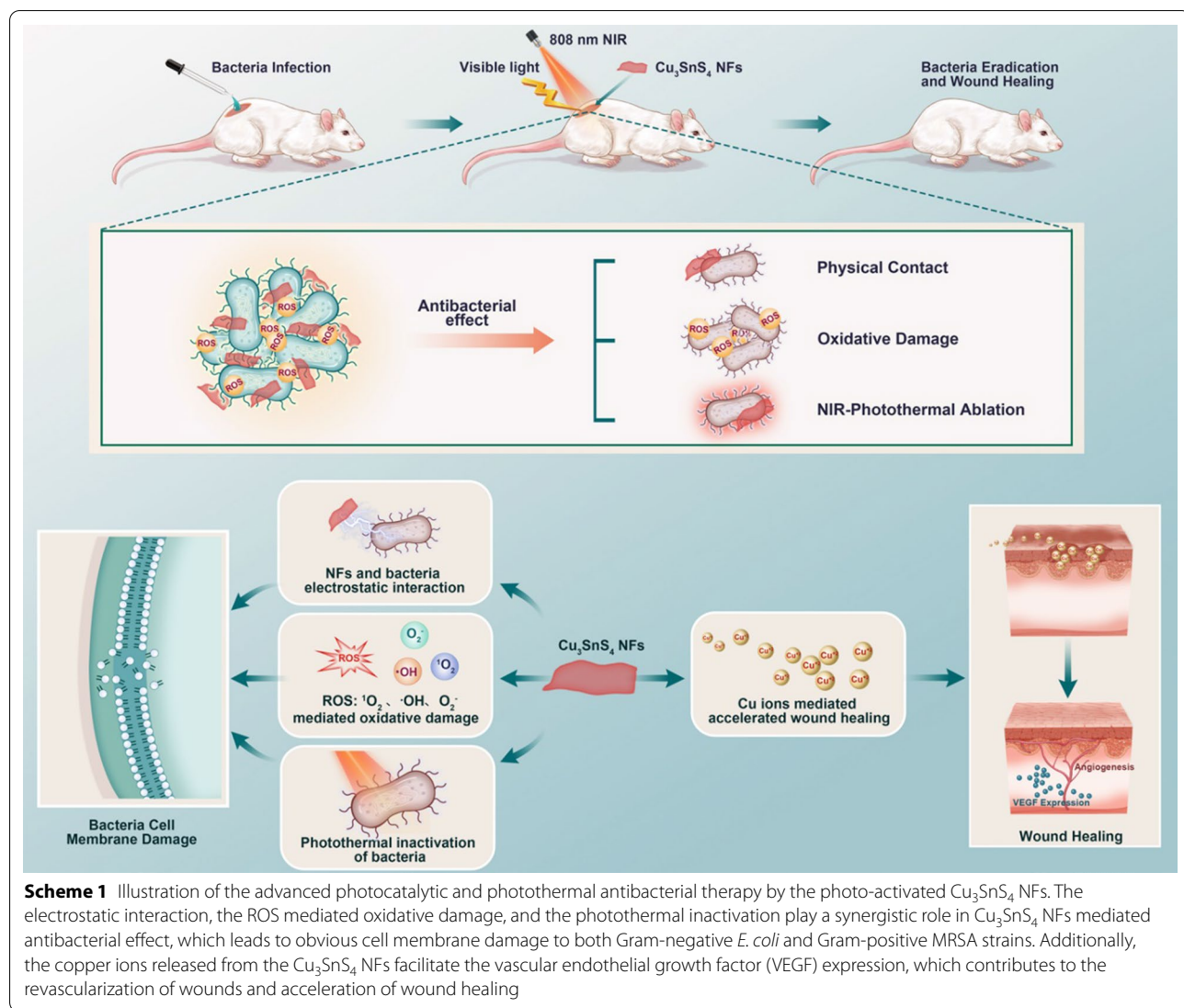
Herein, we presented a facile and low-cost fabrication procedure for Cu₃SnS₄ nanoflakes (NFs) and proposed a Vis-mediated photocatalytic and NIR-activated photothermal synergistic therapeutic strategy for combating the infections of both Gram-negative *Escherichia coli* (*E. coli*) and Gram-positive methicillin-resistant *Staphylococcus aureus* (MRSA) strains (Scheme 1). The underlying antibacterial mechanism was carefully investigated and it was proposed that the ROS mediated cellular oxidative damage and NIR mediated photothermal disruption of bacterial membranes as well as physical contact collaboratively led to the advanced antibacterial therapy. A mouse skin defect and epidermal infected model were established in vivo, showing effective bacteria eradication and favorable healing effects with negligible biotoxicity. Moreover, the inherent localized surface plasmon resonance (LSPR) effect of Cu₃SnS₄ NFs empowered them as an active substrate for surface-enhanced Raman

scattering (SERS) imaging and SERS-labeled bacteria detection. Overall, the low cost and biocompatibility together with the solar-driven broad-spectrum photocatalytic/photothermal antibacterial property of Cu₃SnS₄ NFs make them a candidate for sensitive bacteria detection and effective antibacterial treatment, showing great potential for future clinic applications.

Results and discussion

Construction and characterization of Cu₃SnS₄ NFs

Cu₃SnS₄ NFs were fabricated via a modified solvothermal procedure (Additional file 1: Scheme S1) [29, 30]. As shown in the transmission electron microscopy (TEM) images in Fig. 1A, nearly monodispersed foliate Cu₃SnS₄ NFs were produced. Notably, these NFs were built up by nanocrystals, as can be seen from the high-resolution TEM images and the selected area electron diffraction (SAED) pattern (Fig. 1B, Additional file 1: Fig. S1 and S2). The element mappings in Fig. 1C indicate that each element of Cu, Sn and S was presented and distributed in the framework of Cu₃SnS₄ NFs uniformly. The energy-disperse X-ray spectrum (EDS) shows the distribution of Cu, Sn and S elements without the presence of any other impurities (Fig. 1D). The atomic ratio of Cu:Sn:S is about 2.4:1:3.26, indicating Cu and S vacancies compared with the stoichiometric ratio of Cu₃SnS₄. The crystal structure of as-prepared Cu₃SnS₄ NFs was further characterized by X-ray diffraction (XRD). As shown in Fig. 1E, the diffraction peaks at 2θ values of 28.5, 47.5, and 56.0 were assigned to the (112), (220) and (132) crystal planes of tetragonal Cu₃SnS₄ (JCPDS card No. 33–0501). No impurities can be found in the XRD pattern, indicating the pure phase of Cu₃SnS₄ without secondary phases. The zeta potential analysis shows that the surface of Cu₃SnS₄ NFs was positively charged (+6.3 mV) in deionized water (Fig. 1F). X-ray photoelectron spectroscopy (XPS) was used to further explore the oxidation state of Cu, Sn and S elements in the Cu₃SnS₄. The XPS survey spectrum reveals the presence of Cu, Sn and S peaks (Additional file 1: Fig. S3). The binding energies of the Cu2p_{3/2} and Cu2p_{1/2} centered at 932.1 eV and 952.1 eV respectively (Fig. 1G-1), which could be typically assigned to Cu⁺ species [31]. Additionally, the Cu2p_{3/2} satellite peak at 942.8 eV could be identified as Cu²⁺ species [31], suggesting the presence of both Cu⁺ and Cu²⁺ species in the Cu₃SnS₄ NFs. The binding energies of the Sn3d_{5/2} and Sn3d_{3/2} centered at 486.8 eV and 495.2 eV respectively (Fig. 1G-2), corresponding to the reported values for Sn⁴⁺ [32]. No evidence of Sn²⁺ (binding energy at 485.2 eV) was detected in the sample. The S2p core-level spectrum indicated the binding energy at 161.9 eV (Fig. 1G-3). Additional peak at 168.9 eV was also

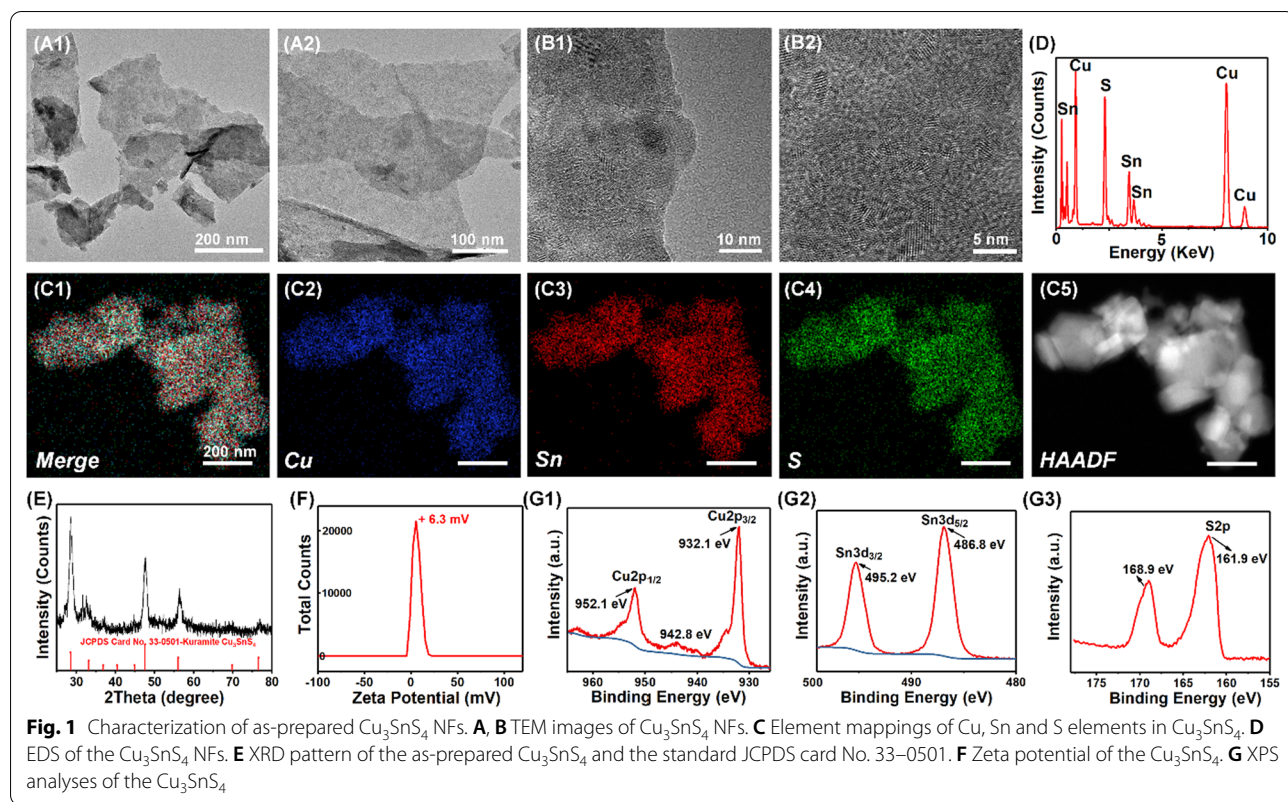


detected, which may be attributed to the oxidized parts of the product.

The photocatalysis mediated ROS generation from Cu_3SnS_4 NFs

As shown in Fig. 2A, the typical optical absorption range of Cu_3SnS_4 NFs crosses from the UV to NIR region (250–1000 nm), highly desirable for full spectrum solar-driven photocatalysis and photothermal antibacterial treatment [33]. The visible light mediated photocatalytic ROS generation was initially evaluated by methylene blue (MB) degradation kinetics, which was monitored by an UV/Vis spectrophotometer. Under visible light irradiation, time-dependent decolorization of MB was observed after incubation with Cu_3SnS_4 NFs for different times (Fig. 2B). The degradation of MB was confirmed by its characteristic absorbance at 664 nm, which decreased with the reaction

proceeding (Fig. 2C). Since both Cu^+ and Cu^{2+} are presented in the Cu_3SnS_4 NFs, it was expected that the Cu ions mediated Fenton-like reaction may boost the ROS generation and further exacerbate the degradation of MB [34]. As observed, the adding of tiny H_2O_2 (1 mM) into the reaction mixture greatly improved the time-dependent degradation efficiency (Fig. 2D, E). It was noted that almost no degradation of MB occurred in 1 mM H_2O_2 solution without the Cu_3SnS_4 catalyst, demonstrating the photocatalysis mediated generation of ROS and degradation of MB. In advanced oxidation technologies, hydroxyl radicals ($\cdot\text{OH}$) are known as one of the key active species for MB degradation with a redox potential of +2.8 V (versus NHE) in acidic media and +1.5 V (versus NHE) in basic media [35]. To test whether $\cdot\text{OH}$ was generated during the Cu_3SnS_4 mediated photocatalytic process,

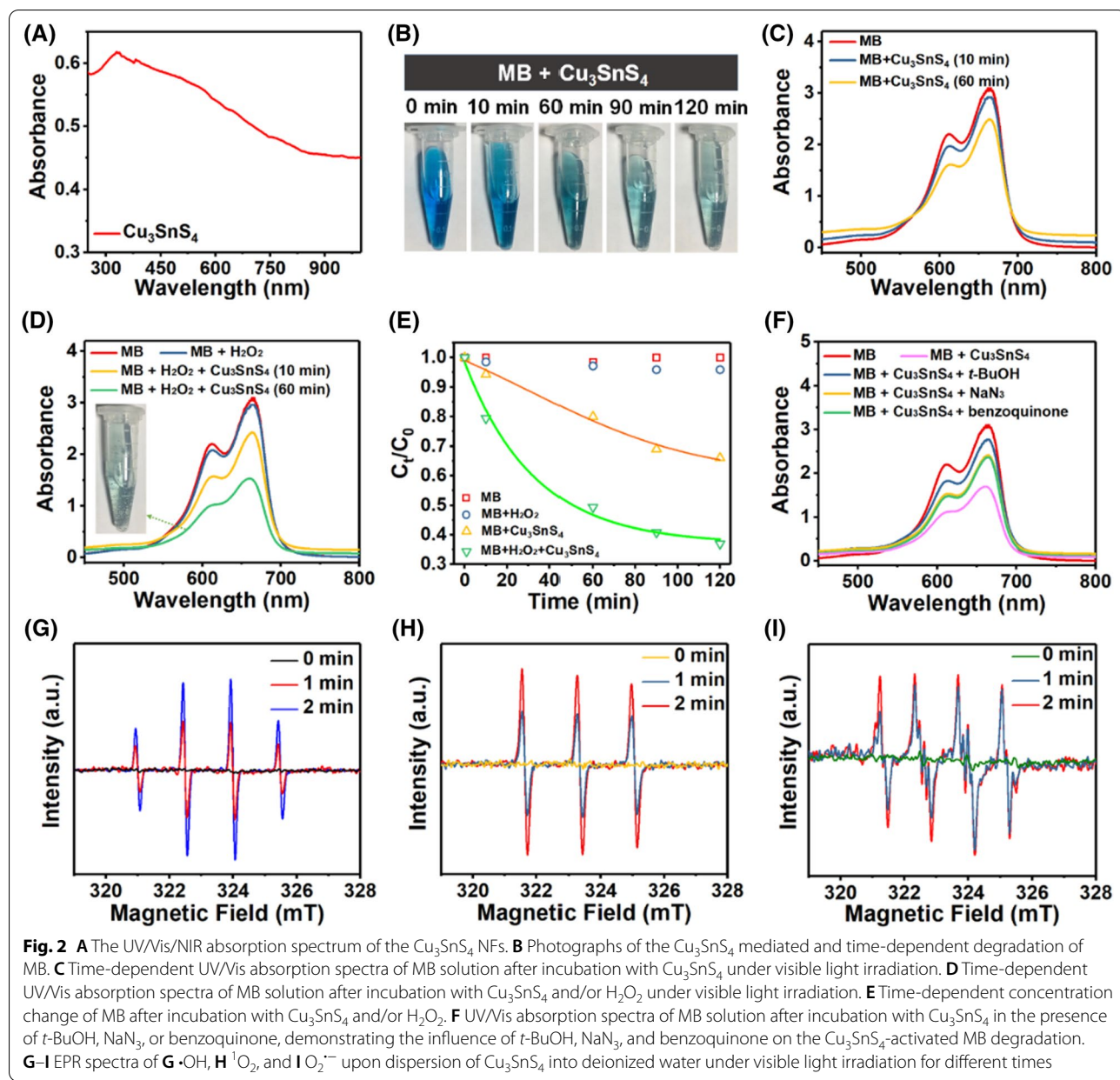


t-butanol (*t*-BuOH), a powerful ·OH scavenger [36], was pre-added to the reaction mixture to investigate whether the degradation could be retarded. It was found that the adding of *t*-BuOH resulted in a concentration-dependent decrease of the MB degradation but not completely quench the reaction (Fig. 2F and Additional file 1: Fig. S4). It is reasonable to speculate that other radical species may be involved in the MB degradation. Here, sodium azide (NaN_3 , 5 mM), a well-known scavenger for the singlet oxygen (${}^1\text{O}_2$) [37, 38], was pre-added to the reaction mixture. As expected, the MB degradation was significantly restrained in the presence of NaN_3 , suggesting the involvement of ${}^1\text{O}_2$ in the Cu_3SnS_4 mediated MB degradation (Fig. 2F). Similarly, the adding of benzoquinone (1 mM), a scavenger of the superoxide radical (O_2^-) [39], also greatly alleviated the MB degradation, indicating the occurrence of O_2^- in the degradation. These data revealed that ·OH, ${}^1\text{O}_2$, and O_2^- possibly occurred and participated in the MB degradation process. In addition, to directly prove the Cu_3SnS_4 mediated ROS generation, the content of ·OH, ${}^1\text{O}_2$, and O_2^- was detected by electron paramagnetic resonance (EPR) using DMPO (5,5-dimethyl-1-pyrroline *N*-oxide) and TEMPO (2,2,6,6-tetramethylpiperidine-1-oxyl) as spin probes [40]. As demonstrated in Fig. 2G–I, the main active species including ·OH, ${}^1\text{O}_2$, and O_2^- could be produced by

the Cu_3SnS_4 NFs under visible light irradiation. Importantly, the amount of ·OH, ${}^1\text{O}_2$, and O_2^- all gradually increased with the prolonged irradiation time. These ROS may further attack bacteria around the photocatalyst and contribute to efficient antibacterial treatment.

The NIR mediated hyperthermia of Cu_3SnS_4 NFs

Cu_3SnS_4 possesses obvious localized surface plasmon resonances (LSPR) in the NIR band [29, 41]. It was speculated that the strong NIR absorption of Cu_3SnS_4 NFs observed in this work could be attributed to LSPR, which may further lead to photothermal effect for antibacterial treatment. Here, different concentrations of Cu_3SnS_4 NFs were dispersed in aqueous solutions and exposed to an 808 nm NIR laser irradiation for different times. Figure 3A–C clearly displays the concentration and irradiation time-dependent photothermal conversion of Cu_3SnS_4 NFs. The solution temperature was precisely controlled between 25 °C and 52 °C by varying the Cu_3SnS_4 concentration or the irradiation time of the NIR light. In contrast, the temperature change of pure water was less than 2 °C under otherwise identical experimental conditions. Importantly, the photothermal conversion of Cu_3SnS_4 NFs was also found to be laser power density-dependent, showing distinct temperature increase when promoting the laser power

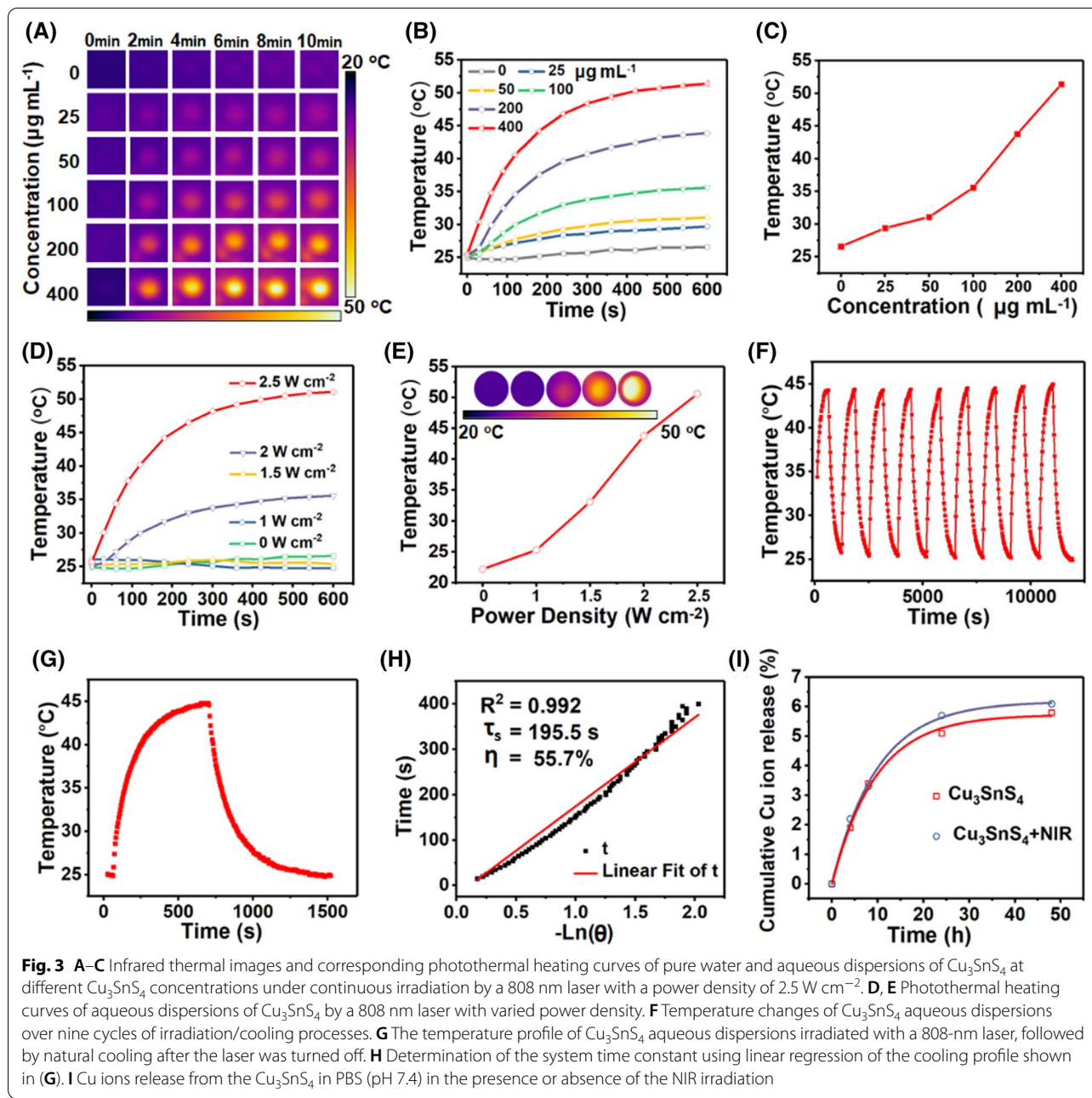


density from 0 W cm^{-2} to 2.5 W cm^{-2} (Fig. 3D, E). Nine successive cycles of heating/cooling processes demonstrated the stable photothermal conversion capability, which is of key importance for photothermal agents during photothermal treatment (Fig. 3F). The photothermal conversion efficiency of Cu_3SnS_4 NFs was calculated to be 55.7% (Fig. 3G, H). The Cu ions released from the Cu_3SnS_4 NFs were evaluated by inductively coupled plasma optical emission spectrometry (ICP-OES). 5.1% of Cu ions was released from the Cu_3SnS_4 NFs within 24 h and 5.8% within 48 h in PBS (pH 7.4), respectively (Fig. 3I). Besides, it was found that the NIR

irradiation ($808 \text{ nm}, 2.0 \text{ W cm}^{-2}, 10 \text{ min}$) did not show distinct interference on the release of Cu ions.

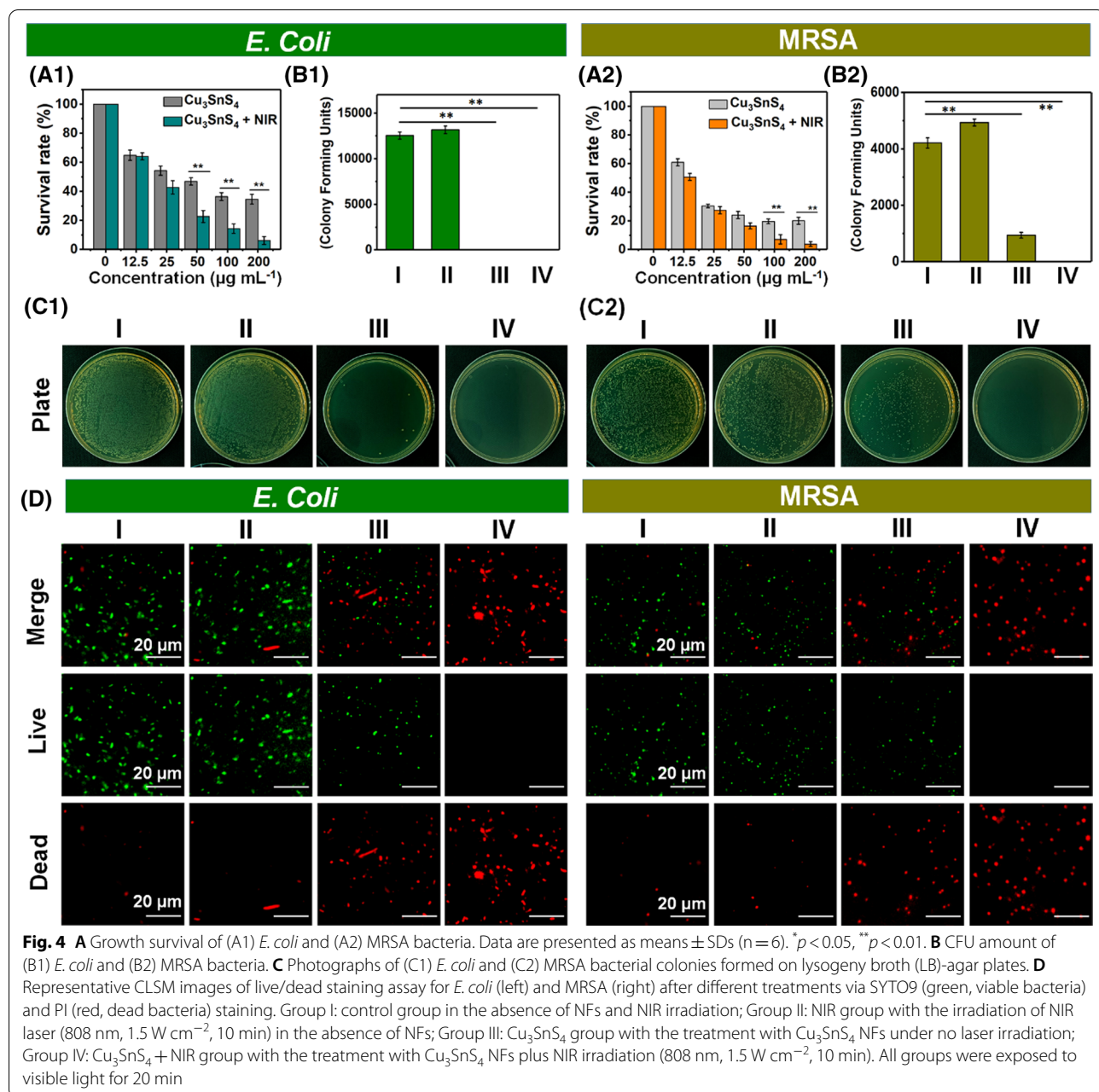
In vitro antibacterial activity

Considering the excellent properties of Cu_3SnS_4 NFs as described above, we set out to examine the possibility of the NFs as a potential photocatalytic agent in combination with the photothermal performance for synergistic elimination of bacteria. Here, the synergistic antibacterial activities of Cu_3SnS_4 NFs against both Gram-negative and Gram-positive bacteria were evaluated using *E. coli* and MRSA as model strains, respectively. The



relative bacterial cells survival was calculated and the colony forming unit (CFU) plate counting method was used to assess the photo-activated disinfection ability of Cu_3SnS_4 NFs (Additional file 1: Fig. S5). As shown in Fig. 4A and Additional file 1: Fig. S6, both bacteria of *E. coli* and MRSA did not show apparent response to only visible light treatment in the absence of the Cu_3SnS_4 NFs and the cell survival was accordingly used as the control group (Group I). In contrast, the bacterial cells survival dramatically decreased to 46.8% (*E. coli*) and 24.1%

(MRSA) after treating with Cu_3SnS_4 at the concentration of $50 \mu\text{g mL}^{-1}$ under visible light for 20 min (Group III), demonstrating the Cu_3SnS_4 NFs mediated inactivation of both bacteria strains. Notably, the bacterial cells survival further decreased to 22.8% (*E. coli*) and 16.5% (MRSA) after the Cu_3SnS_4 plus 808 nm NIR treatment (10 min) under otherwise identical conditions (Group IV). Since NIR alone (Group II, 808 nm, 1.5 W cm^{-2} , 10 min) did not show any antibacterial effect against both strains (Additional file 1: Fig. S7), the enhanced antibacterial



effect after the Cu_3SnS_4 plus NIR treatment thus could be attributed to the NIR activated and synergistic photo-thermal effect of Cu_3SnS_4 . Moreover, the photo-activated disinfection activity of Cu_3SnS_4 NFs could be further enhanced by increasing the dose of the NFs (Fig. 4A). The bacterial cells survival further decreased to 36.4% for *E. coli* and 19.6% for MRSA when promoting the Cu_3SnS_4 NFs dose to $100 \mu\text{g mL}^{-1}$. The CFU plate counting provides a more intuitive characterization of the disinfection ability of Cu_3SnS_4 NFs (Fig. 4B, C). The antibacterial results under only NIR laser irradiation (group II) was

almost the same as that in the control group (group I). In contrast, with the Cu_3SnS_4 NFs treatment, a drastic decrease of MRSA colonies was observed and even no *E. coli* colonies could be detected under only visible light irradiation for 20 min (group III). More significant disinfection efficiency and complete inhibition of bacterial growth were detected in both bacterial models after the Cu_3SnS_4 NFs plus NIR treatment (group IV), demonstrating the remarkable antibacterial ability of photo-activated Cu_3SnS_4 NFs (Fig. 4B, C). The tiny Cu ions released from the Cu_3SnS_4 NFs were found to play

a negligible role on the antibacterial activity of the NFs, as verified by the extract liquid results (Additional file 1: Fig. S8). Fluorescence staining of live/dead cells was performed to further verify the feasibility of eliminating bacteria with different treatments. As shown in the confocal laser scanning microscopy (CLSM) images in Fig. 4D, compared with the green fluorescence displayed in both the control group (group I) and the NIR group (group II), a number of dead cells (red fluorescence) were clearly detected in both strains after incubation with Cu_3SnS_4 NFs even without laser irradiation (group III), which was consistent with the bacterial cell survival results. As expected, treatment with Cu_3SnS_4 NFs plus NIR irradiation induced almost complete death of both bacterial cells, indicating their synergistic and stronger cell-killing effect (group IV).

In this study, we rationalized the efficient antimicrobial activity of Cu_3SnS_4 NFs on the basis of the photocatalysis-mediated ROS generation, which further induced the oxidative stress to kill bacterial cells. To highlight this

property, the ROS level in MRSA bacterial cells were explored by 2',7'-dichlorodihydrofluorescein diacetate (DCFH-DA) staining, which acts as a commonly used method to evaluate the overall oxidative stress level in cells. As exhibited in Fig. 5A and Additional file 1: Fig. S9, bacteria treated with Cu_3SnS_4 NFs with or without NIR irradiation displayed an elevated level of intracellular ROS, which may contribute to the observed antibacterial efficacy of Cu_3SnS_4 NFs. Since both Cu^+ and Cu^{2+} are presented in the Cu_3SnS_4 NFs, it was expected that the Cu ions mediated Fenton-like reaction together with the visible light mediated photocatalysis may collaboratively result in the ROS overproduction (Fig. 5B). To further investigate the antibacterial mechanism of photo-activated Cu_3SnS_4 NFs, the cell morphologies of both *E. coli* and MRSA following different treatments were studied by scanning electron microscopy (SEM, Fig. 5C). Indeed, in contrast to the well-maintained cell morphology in the control group (group I) and NIR group (group II), distorted cell morphology with lesions and holes on

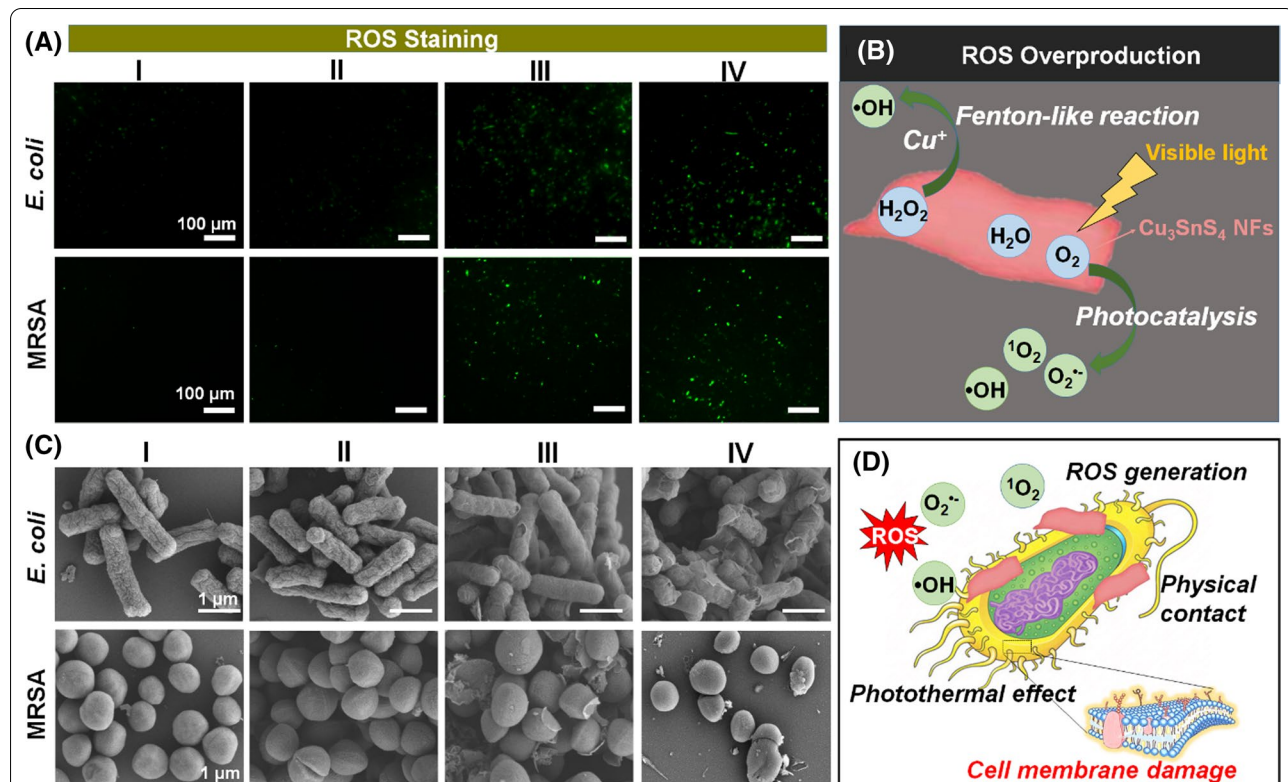


Fig. 5 **A** Intracellular ROS level indicated by DCFH-DA fluorescence staining after diverse treatments. **B** Scheme of the ROS overproduction induced by the Cu ions mediated Fenton-like reaction and the visible light mediated photocatalytic process. **C** SEM micrographs of *E. coli* and MRSA after different treatments. **D** Scheme of the interaction of the physical contact, ROS generation and photothermal effects, which collaboratively led to the damage of bacteria cell membrane. Group I: control group in the absence of NFs; Group II: NIR group with the irradiation of NIR laser (808 nm, 1.5 W cm^{-2} , 10 min) in the absence of NFs; Group III: Cu_3SnS_4 group with the treatment with Cu_3SnS_4 NFs under no laser irradiation; Group IV: Cu_3SnS_4 + NIR group with the treatment with Cu_3SnS_4 NFs plus NIR irradiation (808 nm, 1.5 W cm^{-2} , 10 min). All groups were exposed to visible light for 20 min

the bacterial cell wall/membranes were observed in both bacterial strains after treatment with Cu_3SnS_4 NFs with or without NIR irradiation (group III and group IV). The photogenerated ROS and hyperthermia were presumed to contribute to the cell membrane damage jointly. Besides, a mass of NFs were discovered on the surface of bacteria. Since the surface of bacteria are commonly negatively charged due to the presence of teichoic acids in the cell wall of Gram-positive bacteria and lipopolysaccharide in the outer membrane of Gram-negative bacteria [19], it could be speculated that the electrostatic interaction between the positively charged NFs and the negatively charged bacteria would facilitate the preferential absorption (physical contact) of NFs and reinforce the photocatalysis-based antibacterial efficacy by compromising bacterial membrane integrity [42] (Fig. 5D).

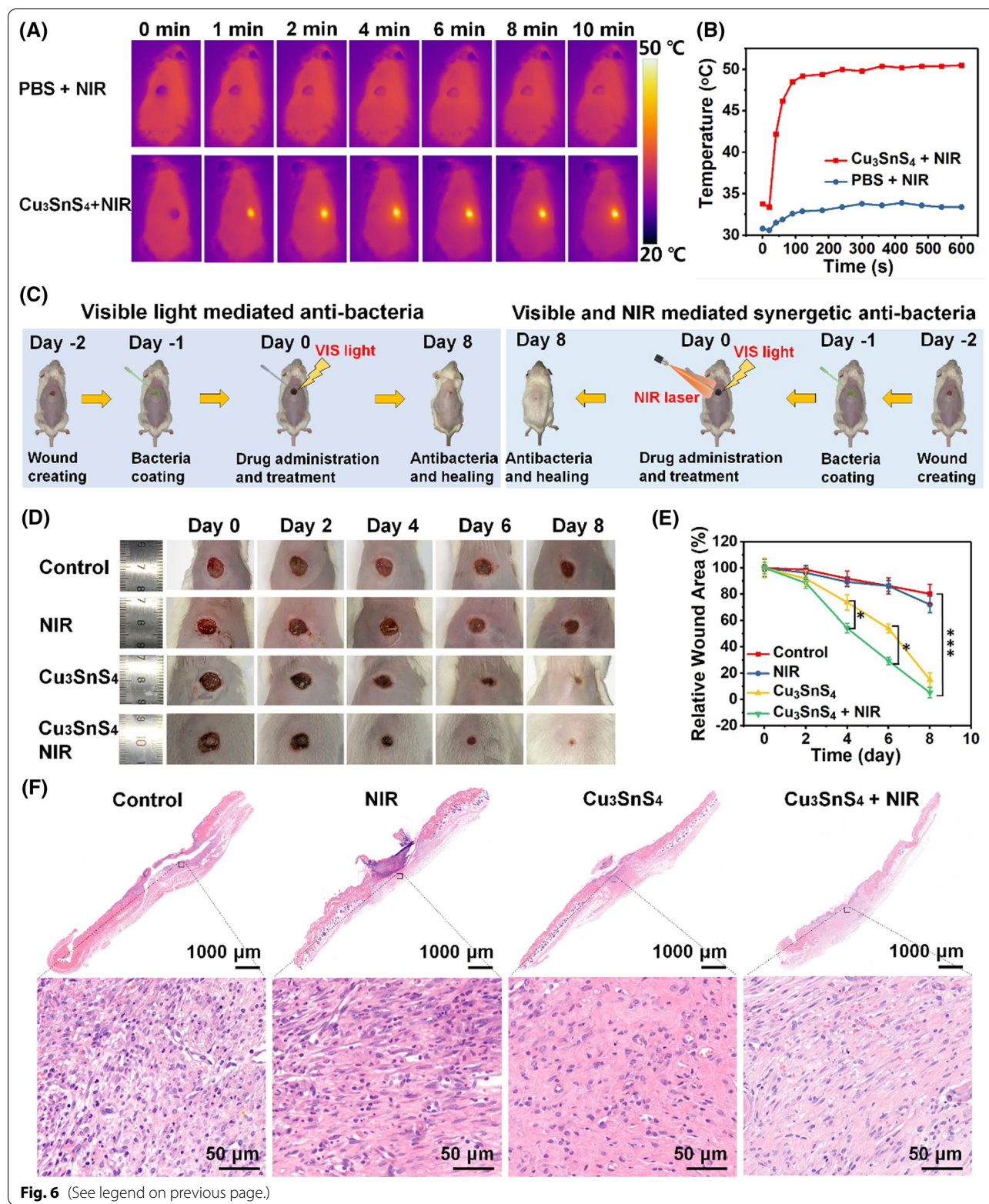
In vivo antibacterial activity

The in vitro biocompatibility of as-prepared Cu_3SnS_4 NFs was evaluated prior to their in vivo biomedical applications. The cytotoxicity of Cu_3SnS_4 NFs to human umbilical vein endothelial cells (HUVEC) and mouse skin fibroblast L929 cells were evaluated, showing no significant toxicity in the wide concentration range of 10–100 $\mu\text{g mL}^{-1}$ within 24 h and 48 h (Additional file 1: Fig. S10). To assess the in vivo antibacterial efficacy of Cu_3SnS_4 NFs, ICR mice with a MRSA-infected cutaneous wound model were fabricated. Initially, the in vivo photothermal effect was explored and shown in Fig. 6A. In contrast to the control group, which showed no distinct change of temperature in the wound area of mice (33.8 °C after 10 min of laser treatment), significantly increased temperature was found in the wound area of the mice treated with Cu_3SnS_4 NFs under the NIR laser irradiation. To be noted, the temperature in the wound area was irradiation time-dependent, which could rapidly reach 49.2 °C in 2 min and maintain around 50 °C in the following 8 min (Fig. 6B). Despite the hyperthermia, no obvious normal tissue damage was observed due to the specific and focused laser irradiation toward the wound area. Then, the photo-activated skin wound-healing ability of Cu_3SnS_4 NFs in wound-infecting mice was evaluated. The treatment process is shown in Fig. 6C. A rounded cutaneous wound model

(6 mm in diameter) was constructed in male ICR mice. Then, MRSA, a common cause of skin infections, was used to construct the wound infecting model. Afterwards, the MRSA-infected mice were divided into four groups ($n=6$ for each group) and treated with (i) PBS (control group), (ii) PBS followed by 808 nm NIR laser irradiation (NIR group), (iii) Cu_3SnS_4 dispersed in PBS (Cu_3SnS_4 group), (iv) Cu_3SnS_4 dispersed in PBS followed by 808 nm NIR laser irradiation ($\text{Cu}_3\text{SnS}_4 + \text{NIR}$ group), respectively. Mice in all groups were exposed to visible light during the treatment. The size of the wound and weight of each mouse were recorded every two days. As shown in Fig. 6D, mice treated with PBS or NIR alone did not show distinct healing of wound despite the presence of scars in both groups (control and NIR group). Significantly, the wound area of mice treated with Cu_3SnS_4 (Cu_3SnS_4 group) was generally smaller, showing around 93.5% recovery on day 8 (Fig. 6E). More importantly, mice treated with Cu_3SnS_4 plus NIR irradiation ($\text{Cu}_3\text{SnS}_4 + \text{NIR}$ group) displayed more pronounced recovery of wound. The trauma area on day 4 has exhibited significant difference as compared to the Cu_3SnS_4 group ($^*p < 0.05$, Fig. 6E), demonstrating the promoted antibacterial and wound healing efficiency based on the collaborative photocatalytic and photothermal antibacterial effects. To further investigate the wound healing process, the wound skin in each group was harvested and exposed to Hematoxylin and eosin (H&E) staining after the treatment. As shown in Fig. 6F, the wound boundary between the wound and normal tissue could be observed clearly from the histological staining results. The keratinocytes migrated to the wound area from the normal tissue and scars became significantly smaller and even vanished after the treatment with Cu_3SnS_4 NFs or Cu_3SnS_4 NFs plus NIR irradiation, whereas incomplete dermal layer was still observed in the control and NIR groups. Besides, the histological slices of both the control group and NIR group presented a number of inflammatory cells, predominantly neutrophils and mononuclear cells adhered to the stratified squamous epithelium. In contrast, intact epidermal layer accompanied with dramatic decrease of the infiltration of inflammatory cells was found after the treatment with Cu_3SnS_4 or Cu_3SnS_4 plus NIR irradiation.

(See figure on next page.)

Fig. 6 **A** In vivo thermal infrared images of mice after different treatments. Mice were treated with PBS or Cu_3SnS_4 NFs followed by NIR laser irradiation for different times. **B** Corresponding temperature change of wounds of mice after treatment with PBS or Cu_3SnS_4 NFs followed by 808 nm laser irradiation. **C** Scheme of the photo-activated antibacterial treatment processes. **D** Representative photographic images of ICR mice with MRSA-infected wounds after different treatments for 8 days: control (treated with PBS), NIR (treated with PBS followed by NIR irradiation), Cu_3SnS_4 (treated with Cu_3SnS_4 NFs), and $\text{Cu}_3\text{SnS}_4 + \text{NIR}$ (treated with Cu_3SnS_4 NFs followed by NIR irradiation). **E** Corresponding changes of wound size in each group during the 8 days' treatments. Data are presented as means \pm SDs ($n=6$). $^*p < 0.05$, $^{***}p < 0.001$. **F** H&E staining of the dermal wound tissues on day 8 after different treatments. For NIR irradiation, 808 nm laser (1.0 W cm^{-2} , 10 min) were used

**Fig. 6** (See legend on previous page.)

plus NIR irradiation, further indicating the efficiency of the photo-activated antibacterial effect of the Cu₃SnS₄ NFs.

In vivo evaluation of collagen deposition and angiogenesis in wounds

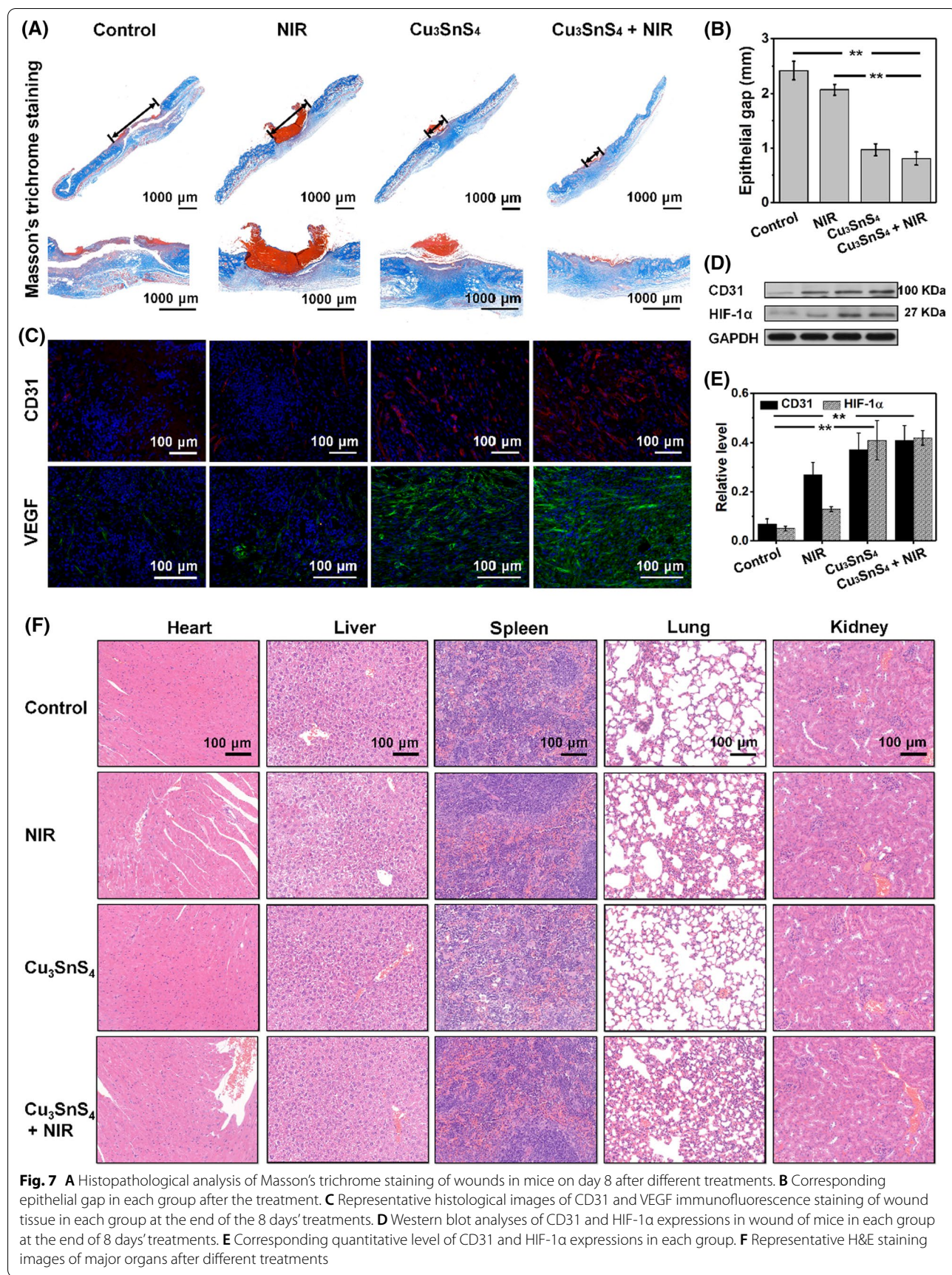
Wound healing is a dynamic process that involves the proliferation of fibroblasts, deposition of collagen fibers, angiogenesis, formation of granulation tissue, scar formation, wound contraction and epithelialization [43]. The synthesis and deposition of collagen is a critical factor in wound healing. Cu ions have been recognized as a cofactor to lysyl oxidase, which stimulates the expression of matrix metalloproteinase-2 and collagen in fibroblasts, facilitating wound healing [44–46]. Histological analysis of Masson's trichrome stained sections showed extensive collagen deposition and a smaller granulation tissue gap in the wounds after the treatment with Cu₃SnS₄ (Fig. 7A, B). Importantly, more wavy collagen fibers were observed in the wounds of the Cu₃SnS₄+NIR group, demonstrating the favourable extracellular matrix remodeling of granulation tissue and regeneration of the epidermis [47]. Further, immunofluorescence staining for CD31, a transmembrane protein expressed early in vascular development, was used to evaluate the newly formed vessels [48]. It showed that the density of newly formed vessels in the wounds of the Cu₃SnS₄ and Cu₃SnS₄+NIR group was more significant compared with the other two groups (Fig. 7C). The Western blot analysis of CD31 was in concordance with the immunofluorescence staining results, further confirming the promoted vessel number after the treatments (Fig. 7D). Moreover, it has been suggested that hypoxia plays a critical role in cell recruitment, cell differentiation and blood vessel formation [49]. Hypoxia inducible factor-1α (HIF-1α) has been identified to initiate the transcription of hypoxia sensitive genes including vascular endothelial growth factor (VEGF) under hypoxic conditions [50]. Stabilization and activation of HIF-1α expression was thus suggested as a potential strategy to promote neovascularization [51]. The HIF-1α expression and VEGF secretion in wounds after the treatment were then investigated, trying to figure out the angiogenesis during the wound healing process. The HIF-1α expression, as determined by the Western blot analysis, was promoted both in the Cu₃SnS₄ and Cu₃SnS₄+NIR group as compared with the other two groups (Fig. 7D, E). Moreover, the immunofluorescence staining of VEGF showed more significant expression of VEGF and therefore more new blood vessel formation after the Cu₃SnS₄ and Cu₃SnS₄+NIR treatment (Fig. 7C). The promotion of angiogenesis was expected to allow more supply of oxygen and nutrients as well as accelerated migration of requisite cells and humoral factors into wounds, which leads subsequently to the increased formation of granulation tissue,

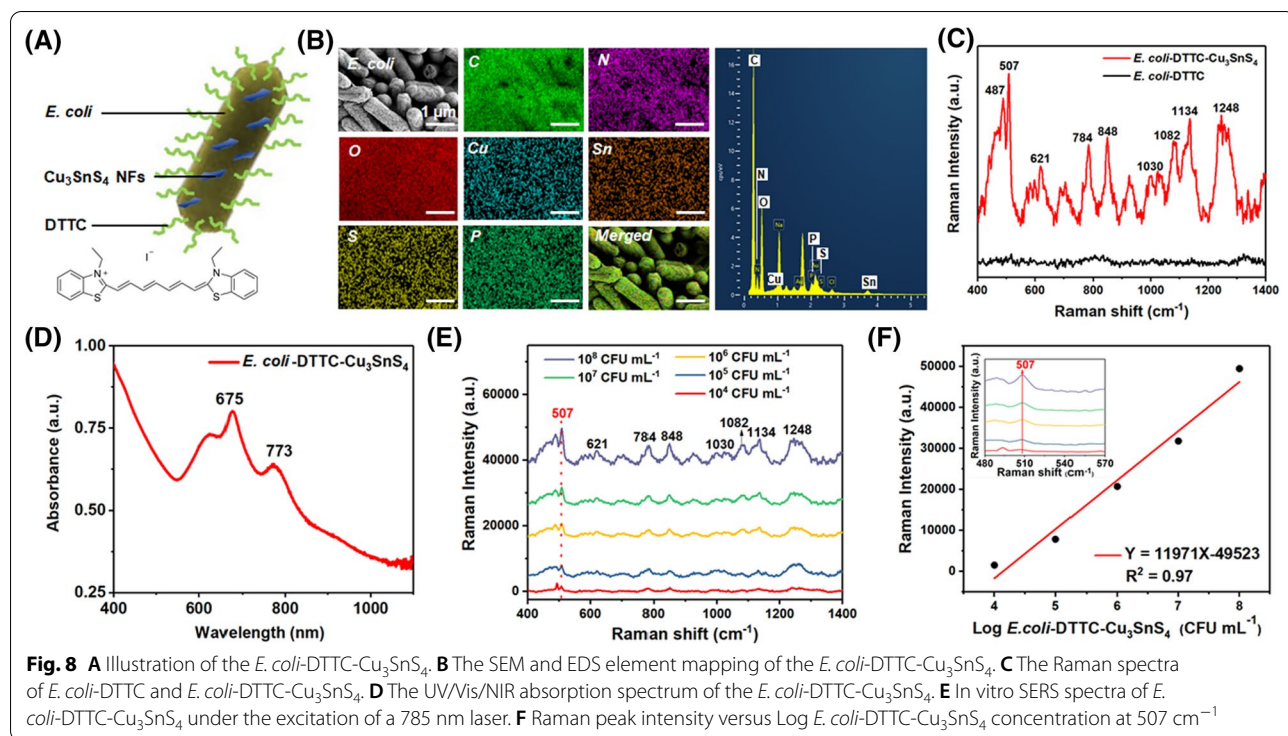
collagen synthesis and eventually improved wound healing [45].

Furthermore, the in vivo biosafety after the Cu₃SnS₄ and/or NIR treatment was evaluated. The body weight of mice in each group during the whole treatment process did not show distinct difference (Additional file 1: Fig. S11). Besides, the main blood biochemistry and hematology analyses of mice in each group after the treatment were conducted, suggesting normal functions in liver and kidney (Additional file 1: Fig. S12). The routine blood test was further assessed to monitor the systemic inflammatory activity, showing no significant differences as compared with the control group (Additional file 1: Fig. S13). Moreover, no visible damage, inflammation, or abnormality were observed in the histological evaluation of major organs including heart, liver, spleen, lung, and kidney (Fig. 7F). Collectively, the biosafety analyses substantiate that the photo-activated antibacterial treatment showed no obvious side-effect to mice in vivo.

Cu₃SnS₄ NFs as an active SERS substrate for the detection of *E. coli* in vitro

Surface-enhanced Raman scattering (SERS) imaging is a highly sensitive tool that allows direct identification of target analytes in proximity to the surface of plasmonic nanoparticles [52]. Due to its high sensitivity, chemical specific, high resolution, and non-destructive characteristics, SERS imaging has demonstrated applications in biomedicine as a promising tool for real-time bacteria detection [53]. Cu₃SnS₄ compound is a p-type semiconductor due to the presence of copper vacancies, which further endows Cu₃SnS₄ with localized surface plasmon resonance (LSPR) in the NIR region [54]. Indeed, a wide absorption band in the NIR region associated with LSPR is clearly observed in the UV/Vis/NIR spectrum of Cu₃SnS₄ NFs. The natural excitation of Cu₃SnS₄ LSPRs in the NIR paves the way for the employment of Cu₃SnS₄ NFs as SERS substrate for enhanced signals of Raman imaging. Here, we set out to explore the possibility of utilizing Cu₃SnS₄ NFs as a SERS substrate for the determination of bacteria content. *E. coli* was used as the model bacteria and tagged with Raman reporter molecules of 3,3'-diethylthiatricarbocyanine iodide (DTTC), followed by the immobilizing of Cu₃SnS₄ NFs (designated as *E. coli*-DTTC-Cu₃SnS₄). The as-prepared *E. coli*-DTTC-Cu₃SnS₄ is illustrated in Fig. 8A. The EDS analysis of the *E. coli*-DTTC-Cu₃SnS₄ showed well-merged element images of C, N, O, P, Cu, Sn, and S elements, confirming the presence of both DTTC and Cu₃SnS₄ on the bacteria. The *E. coli*-DTTC-Cu₃SnS₄ were subsequently exposed to a 785 nm laser with 10 mW laser power, 5 s acquisition time, and a 50× object lens. Significant enhancement of characteristic Raman signals





of the DTTC molecule around 507 , 621 , 784 , 848 , 1082 , 1134 , and 1248 cm^{-1} was observed after the coupling of Cu_3SnS_4 NFs [55, 56], while negligible Raman signal was captured in equivalent *E. coli*-DTTC without Cu_3SnS_4 nanostructure (Fig. 8C). This result clearly demonstrates the possibility of Cu_3SnS_4 NFs as SERS substrate for the enhancement of Raman probe signals. As can be seen from the UV/Vis/NIR spectrum of *E. coli*-DTTC- Cu_3SnS_4 (Fig. 8D and Additional file 1: Fig. S14), the LSPR peak of *E. coli*-DTTC- Cu_3SnS_4 was in proximity with the wavelength of the excitation laser for SERS imaging (785 nm). The enhancement thus could be attributed to the LSPR on the Cu_3SnS_4 NFs under the excitation of 785 nm laser beam, which strengthened local electromagnetic field and led to enhanced Raman probe signals [57]. We subsequently demonstrate the high sensitivity of utilizing Cu_3SnS_4 NFs for SERS based *E. coli* detection. A series of *E. coli* tagged with DTTC at concentrations from 10^8 CFU mL^{-1} to 10^3 CFU mL^{-1} were coupled with Cu_3SnS_4 NFs, followed by subjection to SERS detection. As shown in Fig. 8E and Additional file 1: Fig. S15, the SERS labeled bacteria with different cell counts from 10^8 CFU mL^{-1} to 10^4 CFU mL^{-1} could be clearly delineated with low signal-to-background ratio. Using the Raman shift of DTTC molecule at 507 cm^{-1} for detection, *E. coli* could be detected at a minimal concentration of 10^4 CFU mL^{-1} . Figure 8F displays the intensity of the SERS peak at 507 cm^{-1} as a function of logarithmic concentrations of *E. coli*-DTTC- Cu_3SnS_4 .

A linear dependence was found with concentrations of *E. coli*-DTTC- Cu_3SnS_4 ranging from 10^4 CFU mL^{-1} to 10^8 CFU mL^{-1} , corresponding to doses of Cu_3SnS_4 ranging from $75.5 \mu\text{M}$ to $325.7 \mu\text{M}$ (Additional file 1: Fig. S16). Compared with common noble metals (Ag and Au) nanostructure-based substrates, the fabrication procedure of Cu-based Cu_3SnS_4 NFs is facile and low-cost, thus representing a promising active substrate for SERS based bacteria detection.

Conclusions

In conclusion, photo-activatable Cu_3SnS_4 NFs were prepared for advanced antibacterial therapy by inducing efficient bacteria eradication and accelerated wound healing. The Cu_3SnS_4 NFs could be activated by visible light, leading to effective overproduction of ROS in bacterial cells. Besides, the high photothermal conversion efficiency of Cu_3SnS_4 NFs induced NIR light (808 nm) controlled hyperthermia in bacteria. Importantly, the electrostatic interaction between the positively charged Cu_3SnS_4 NFs and the negatively charged bacteria facilitated the physical contact mediated bacteria killing. Consequently, the physical contact and ROS mediated cellular oxidative damage as well as the NIR mediated photothermal disruption of bacterial membranes played a synergistic role in the efficient eradication of both *E. coli* and MRSA in vitro and in vivo. On the other hand, the exogenous ions metabolism from

the Cu₃SnS₄ NFs significantly up-regulated the expression of HIF-1α, CD31 and VEGF, leading to increased formation of granulation tissue, collagen synthesis and eventually improved wound healing. Additionally, the Cu₃SnS₄ NFs can be used as an active SERS imaging substrate for SERS-labeled bacteria detection *in vitro*. The sensitive bacteria detection and the solar-driven broad-spectrum antibacterial therapeutic effects as well as the high biocompatibility and therapeutic biosafety endow Cu₃SnS₄ NFs with potentiality for future clinical transformation.

Methods

Materials

Copper acetate hydrate (CuAc₂·H₂O), stannic chloride pentahydrate (SnCl₄·5H₂O), hydrogen peroxide (H₂O₂, 30 wt%), thioacetamide (TAA), and N,N-dimethylformamide (DMF) were obtained from Sinopharm Chemical Reagent Co., Ltd. Sodium azide (NaN₃), *t*-butanol (*t*-BuOH), benzoquinone, and methylene blue (MB) were purchased from Aladdin Chemical Reagent Co., Ltd. 5,5-dimethyl-1-pyrroline N-oxide (DMPO) and 2,2,6,6-tetramethyl-piperidine-1-oxyl (TEMPO) were bought from Adamas Reagent, Ltd. All reagents were purchased as received and used without any further purification.

Preparation and characterization of Cu₃SnS₄ NFs

The Cu₃SnS₄ NFs were prepared by a facile solvothermal strategy. In a typical synthesis, 0.06 mmol CuAc₂·H₂O, 0.04 mmol SnCl₄·5H₂O and 0.08 mmol thioacetamide (TAA) were mixed in 10 ml N,N-dimethylformamide (DMF). The mixture was purged with argon and stirred for 2 h under 140 °C. Then, the reaction mixture was transferred to a stainless-steel autoclave and the reaction was processed at 220 °C for 12 h. After completing the reaction, the mixture was naturally cooled to room temperature and centrifuged at 5000 rpm for 10 min. The precipitate was washed with acetone and deionized water to remove by-products. The obtained black powder was dried at 80 °C for 12 h and used for further characterization.

Characterization

Transmission electron microscopy (TEM), high resolution-TEM (HRTEM), energy dispersive X-ray spectroscopy (EDS), and the corresponding element mapping analyses were conducted on a JEM-2100F electron microscope. Zeta potential was determined on Malvern Zetasizer Nanoseries (Nano ZS90). X-ray photoelectron spectroscopy (XPS) was acquired on an Axis Ultra DLD spectrometer (Kratos, UK). UV-visible (UV/Vis) absorbance spectra were obtained on a UV-3101 Shimadzu spectroscope. The quantitative elemental analysis was carried

out on an inductively coupled plasma optical emission spectrometer (ICP-OES, Agilent 700 Series, USA). Powder X-ray diffraction (XRD) pattern was tested on a Rigaku Ultima IV diffractometer. The electron paramagnetic resonance (EPR) was conducted on a Bruker EMXplus X-band EPR.

The photocatalysis mediated ROS generation from Cu₃SnS₄ NFs

The photocatalysis mediated ROS generation was evaluated using the methylene blue (MB) probe. Briefly, 4 mL of methylene blue (MB, 10 µg mL⁻¹) aqueous solution was added to 6 mL of the aqueous solution containing 0.6 mg of Cu₃SnS₄ NFs and shaken slightly under light. 0.5 mL of the reaction suspension was then taken out, diluted with water, and detected by a UV/Vis spectrometer at 664 nm periodically. The MB degradation process was also photographed. To investigate the Cu ions mediated Fenton-like reaction, 1 mL of H₂O₂ aqueous solution (1 mM) was immediately added to the above solution and the MB degradation was evaluated with a similar procedure.

Additionally, using DMPO and TEMPO as spin probes, the photocatalysis mediated ROS (including ·OH, ¹O₂, and O₂^{·-}) generation was further detected by electron paramagnetic resonance (EPR). Typically, 0.1 mg of Cu₃SnS₄ NFs were added to 10 mL of deionized water under dark conditions. The suspension was then exposed to visible light irradiation and the EPR signal of the complex of ·OH, ¹O₂, and O₂^{·-} with the probes was captured periodically (0, 1 and 2 min).

The NIR mediated hyperthermia of Cu₃SnS₄ NFs

The NIR mediated hyperthermia and the photothermal efficiency of the Cu₃SnS₄ NFs were investigated using an 808 nm fiber-coupled laser system. Briefly, different concentrations of Cu₃SnS₄ dispersions (0, 25, 50, 100, 200 and 400 µg mL⁻¹) were irradiated by an 808 nm fiber-coupled laser system for different times (0, 2, 4, 6, 8 and 10 min) at varied power density (0, 1, 1.5, 2 and 2.5 W cm⁻²). The temperature of the suspensions was recorded every 50 s with an IR camera to analyze the temperature elevation tendency. The photothermal stability of Cu₃SnS₄ NFs was evaluated by turning on the NIR laser (808 nm, 2.0 W cm⁻²) for 10 min and then off until the dispersions reached room temperature periodically. Nine circulations were recorded.

The photothermal conversion efficiency (η) was calculated using the following equations:

$$\eta = \frac{hS(T_{Max} - T_{Sur}) - Q_{Dis}}{I(1 - 10^{-A808})}$$

$$hs = \frac{m_D C_D}{\tau_s}$$

In these equations, m_D represents the solution mass and equals to 0.2 g, while $C_D = 4.2 \text{ J g}^{-1}$ is the heat capacity of water. $T_{Max} = 42.15 \text{ }^\circ\text{C}$ and $T_{Surr} = 25 \text{ }^\circ\text{C}$ are the maximum temperature of the NFs and the water during the irradiation process, respectively. Q_{Dis} is associated with the light absorbance of the solvent, which approximately equals to 0. τ_s is the irradiation time during the temperature rise and equals to 195.5 s. I is the laser power and equals to 2.0 W cm^{-2} . $A_{808} = 0.47$ is the absorbance of the NFs at 808 nm. The photothermal conversion efficiency was thus calculated to be 55.7%.

The Cu ions released from the Cu_3SnS_4 NFs were investigated by ICP-OES analysis. Typically, 0.5 mg of Cu_3SnS_4 NFs were added to 10 mL of deionized under dark conditions at room temperature. The Cu ions release process was performed on a shaking table at a shaking speed of 180 rpm. At each time point, 1 mL of the supernate was taken out, filtrated, diluted, and measured by ICP-OES. To investigate the NIR mediated Cu ions release, the suspension was exposed to NIR irradiation (808 nm, 2.0 W cm^{-2}) for 10 min.

In vitro cytotoxicity of Cu_3SnS_4 NFs

Human umbilical vein endothelial cells (HUVECs) and mouse fibroblast cells (L929) were obtained from the China Center of Industrial Culture Collection. Cells were seeded separately into 96-well plates at $6 \times 10^4 \text{ cells mL}^{-1}$. The cells were incubated in α -MEM with 10% FBS at $37 \text{ }^\circ\text{C}$ in 5% CO_2 atmosphere. After 24 h, the original media was removed, and α -MEM containing a diverse concentration of Cu_3SnS_4 NFs (0, 10, 25, 50, $100 \mu\text{g mL}^{-1}$) was added to the plates. Cytotoxicity was detected after 24 h and 48 h co-culture using the CCK-8 method. The optical density (OD) of each solution was tested at 490 nm using an ELX-800 absorbance microplate reader.

In vitro bacterial cell culture

Gram-negative *E. Coli* (ATCC 25,922) and Gram-positive methicillin-resistant *S. aureus* (MRSA, ATCC 43,300) were obtained from American Type Culture Collection (ATCC). *E. coli* (ATCC 25,922) and MRSA (ATCC 43,300) were initially seeded on solid Luria–Bertani Broth medium with streak plate method. After being cultured at $36 \text{ }^\circ\text{C}$ for 24 h, we collected a single bacterial colony and immerged it into 10 mL of liquid Luria–Bertani Broth medium separately for further cultivation. The centrifuge tubes were placed in a shaking incubator at 100 rpm at $30 \text{ }^\circ\text{C}$ for 20 h. Cells were then centrifuged

(5000 rpm, 10 min, $4 \text{ }^\circ\text{C}$) and washed with PBS for three times before use.

The evaluation of antibacterial activity of Cu_3SnS_4 NFs in vitro

The antibacterial probability of Cu_3SnS_4 NFs was measured with the spread plate method. The solution was concentrated using a centrifuge (5000 rpm, 10 min, $4 \text{ }^\circ\text{C}$) and the supernatant was removed. Next, the pellets were resuspended and diluted at a density of $1 \times 10^5 \text{ CFU mL}^{-1}$ with PBS (pH 6.0) containing Cu_3SnS_4 NFs at $100 \mu\text{g mL}^{-1}$ and $0 \mu\text{g mL}^{-1}$, according to the optical density (OD) value tested at 650 nm. Each concentration of solution underwent various disposal: I. Control: A suspension containing $0 \mu\text{g mL}^{-1}$ of Cu_3SnS_4 NFs, irradiated with steady light. II. A suspension containing $0 \mu\text{g mL}^{-1}$ of Cu_3SnS_4 NFs, irradiated with steady light and NIR laser (808 nm, 2.0 W cm^{-2} , 10 min). III. A suspension containing $100 \mu\text{g mL}^{-1}$ of Cu_3SnS_4 NFs, irradiated with steady light. IV: A suspension containing $100 \mu\text{g mL}^{-1}$ of Cu_3SnS_4 NFs, irradiated with steady light and NIR laser (808 nm, 2.0 W cm^{-2} , 10 min). After the procedure, 100 μl of each diluted suspension was spread onto the solid Luria–Bertani Broth medium, incubated at $37 \text{ }^\circ\text{C}$ in 5% CO_2 overnight. The number of bacterial colonies was then counted.

In vitro fluorescence live/dead staining of bacteria

The bacterial suspensions were prepared in different methods: I. PBS. II. PBS + NIR laser (808 nm, 2.0 W cm^{-2} , 10 min). III. Cu_3SnS_4 NFs ($100 \mu\text{g mL}^{-1}$). IV. Cu_3SnS_4 NFs ($100 \mu\text{g mL}^{-1}$) + NIR laser (808 nm, 2.0 W cm^{-2} , 10 min). Before staining, the supernatant containing bacterial cells was collected and centrifuged to remove Cu_3SnS_4 NFs. The supernatant was also discarded to remove nucleic acids or other media components that might decrease staining efficiency. Then we resuspended the pellets with sterile water containing 0.85% NaCl, SYTO9 (10 μM) and PI (10 μM). The suspension was incubated in the dark for 15 min. The stained cells were transferred to confocal dishes. Fluorescent images of the live (green fluorescent) and dead (red fluorescent) cells were obtained using an Olympus confocal laser scanning microscope.

Morphology observation of bacteria by bio-SEM

After the anti-bacteria test, cell morphology images were acquired by SEM scanning. The bacterial suspensions: I. PBS. II. PBS + NIR laser (808 nm, 2.0 W cm^{-2} , 10 min). III. Cu_3SnS_4 NFs ($100 \mu\text{g mL}^{-1}$). IV. Cu_3SnS_4 NFs ($100 \mu\text{g mL}^{-1}$) + NIR laser (808 nm, 2.0 W cm^{-2} , 10 min) were fixed with 2.5% glutaraldehyde overnight at $4 \text{ }^\circ\text{C}$. All samples were centrifuged and resuspended with PBS

(0.1 M) for four times. Then all samples were fixed with osmic acid (1%, pH 7.3) for 1 h. Before dehydration, samples were washed with PBS (0.1 M) and ultrapure water for two times. Graded alcohol (30%, 50%, 60%, 70%, 80%, 90%, 100%, 100%, and 100%) was applied to dehydrate the bacteria. During each procedure, the pellets were mixed with solution thoroughly for 10 min. All samples were dried using the supercritical CO₂ drying technology. The bacteria morphology was visualized using bio-SEM.

Animals

Male ICR mice aged 5 weeks were obtained from Shanghai Super-B&K laboratory animal Corp. Ltd. The Institutional Animal Care and Use Committee of Shanghai Ninth People's Hospital, Shanghai Jiao Tong University School of Medicine approved all the animal study protocols. All animal experiments were carried out in agreement with the guidelines of Shanghai Laboratory Animal Research Center.

In vivo wound disinfection and healing assay

The ICR mice were divided into four groups, and each group consists of four mice. All mice were raised in cages under the same condition. First, the mice were injected with 5% chloral hydrate in the abdominal cavity. After anesthesia took effect, a circular wound in 6 mm was prepared on the back of each mouse with a skin punch. One day after the wound was created, 50 μL of MRSA solution (2×10^8 CFU mL⁻¹) was dropped into each wound to construct the wound healing model. According to the grouping, various treatments were operated: I. PBS. II. PBS + NIR laser (808 nm, 1.0 W cm⁻², 10 min). III. Cu₃SnS₄ NFs (100 μg mL⁻¹). IV. Cu₃SnS₄ NFs (100 μg mL⁻¹) + NIR laser (808 nm, 1.0 W cm⁻², 10 min). Meantime, an IR camera was deployed to record thermal images. Body weights and wound sizes were recorded every 2 days post wounding until all mice were sacrificed on the 8th day after treatment. Meanwhile, in vivo biosafety and wound healing was investigated through HE staining, mason's trichrome staining, and immunofluorescence staining (CD31, VEGF), utilizing skin tissues and main organs (liver, spleen, lung, and kidney) harvested. For the Western blot analyses, formalin-fixed, paraffin-embedded (FFPE) skin wound samples were sectioned at a thickness of 10 μm. After sections were dewaxed by adding 500 μL of octane and vigorously shaken for 10 s, 750 μL methanol was added and shaken for another 10 s. Samples were then centrifuged (15,000 g, 10 min, 4 °C) to remove the upper suspension, and pellets were dried for 5 min. 50 μL of lysis buffer containing 20 mM Tris-HCl (pH 7.4) and 2% SDS was added, followed by

heating at 100 °C for 20 min and 60 °C for 2 h. Samples were then collected and went through western blot assay. Expression variation of CD31 and HIF-1α was tested.

Supplementary Information

The online version contains supplementary material available at <https://doi.org/10.1186/s12951-022-01403-y>.

Additional file 1: Scheme S1. Illustration of the preparation process of Cu₃SnS₄ NFs. **Figure S1.** HRTEM image of the Cu₃SnS₄ NFs. **Figure S2.** The selected area electron diffraction (SAED) pattern of the Cu₃SnS₄ NFs. **Figure S3.** The XPS survey spectrum of the Cu₃SnS₄ NFs. **Figure S4.** Influence of t-BuOH to the Cu₃SnS₄ NFs mediated methylene blue degradation. Conditions: 10 μg mL⁻¹ methylene blue, 100 μg mL⁻¹ Cu₃SnS₄ NFs, t = 120 min, 25 °C. **Figure S5.** Illustration of the process of antibacterial experiment *in vitro*. **Figure S6.** Photographs of *E. coli* and MRSA bacterial colonies formed on lysogeny broth (LB)-agar plates under visible light irradiation for different times. (B) Corresponding CFU amount of *E. coli* and MRSA bacteria after visible light irradiation for different times. **Figure S7.** (A) Photographs of *E. coli* and MRSA bacterial colonies formed on lysogeny broth (LB)-agar plates under NIR irradiation (808 nm, 10 min) with different power density. (B) Corresponding CFU amount of *E. coli* and MRSA bacteria after NIR irradiation (808 nm, 10 min) with different power density. **Figure S8.** (A) Photographs of *E. coli* and MRSA bacterial colonies formed on lysogeny broth (LB)-agar plates. I: *E. coli*, II: *E. coli* after the treatment with Cu ions extract liquid, III: MRSA IV: MRSA after the treatment with Cu ions extract liquid. (B) Corresponding CFU amount of *E. coli* and MRSA bacteria after different treatments. **Figure S9.** Relative fluorescence intensity of DCF in MRSA after different treatments. Data are presented as means ± SDs (n = 4). **p < 0.01. Group I: control group in the absence of NFs; Group II: NIR group with the irradiation of NIR laser (808 nm, 1.5 W cm⁻², 10 min) in the absence of NFs; Group III: Cu₃SnS₄ group with the treatment with Cu₃SnS₄ NFs under no laser irradiation; Group IV: Cu₃SnS₄ + NIR group with the treatment with Cu₃SnS₄ NFs plus NIR irradiation (808 nm, 1.5 W cm⁻², 10 min). All groups were exposed to visible light for 20 min. **Figure S10.** Relative cell viability of HUVEC and L929 cells after treatment with Cu₃SnS₄ NFs (0–100 μg mL⁻¹) for 24 h and 48 h under dark conditions. Data are presented as means ± SDs (n = 4). **Figure S11.** Time dependent change of body weight of mice after different treatments. Data are presented as means ± SDs (n = 6). **Figure S12.** *In vivo* hematological index (AST, ALT, BUN, and CREA) of male ICR mice on day 8 after different treatments. Data are presented as means ± SDs (n = 6). Group I: control group in the absence of NFs; Group II: NIR group with the irradiation of NIR laser (808 nm, 1.0 W cm⁻², 10 min) in the absence of NFs; Group III: Cu₃SnS₄ group with the treatment with Cu₃SnS₄ NFs under no laser irradiation; Group IV: Cu₃SnS₄ + NIR group with the treatment with Cu₃SnS₄ NFs plus NIR irradiation (808 nm, 1.0 W cm⁻², 10 min). All groups were exposed to visible light during the treatment. **Figure S13.** The major hematological indicators of healthy male ICR mice on day 8 after different treatments. Data are presented as means ± SDs (n = 6). Group I: control group in the absence of NFs; Group II: NIR group with the irradiation of NIR laser (808 nm, 1.0 W cm⁻², 10 min) in the absence of NFs; Group III: Cu₃SnS₄ group with the treatment with Cu₃SnS₄ NFs under no laser irradiation; Group IV: Cu₃SnS₄ + NIR group with the treatment with Cu₃SnS₄ NFs plus NIR irradiation (808 nm, 1.0 W cm⁻², 10 min). All groups were exposed to visible light during the treatment. **Figure S14.** The UV/Vis/NIR absorption spectra of the *E. coli*, DTTC and *E. coli*-DTTC-Cu₃SnS₄. **Figure S15.** *In vitro* SERS spectra of *E. coli*-DTTC-Cu₃SnS₄ under the excitation of a 785 nm laser. **Figure S16.** The concentration of Cu in the *E. coli*-DTTC-Cu₃SnS₄, which is positively related to the concentration of the *E. coli*.

Acknowledgements

We thank the Instrumental Analysis Center of Shanghai Jiao Tong University for materials testing.

Author contributions

YH, JF and YY designed the experiments. YY and JF performed the synthesis and characterization of the materials. YY and CW performed the *in vitro* experiments. YY, JF, and JL participated in the *in vivo* experiments. NW, JL, YZ and JZ contributed to data analysis. YY, JF and YH contributed to the manuscript preparation. All authors read and approved the final manuscript.

Funding

We acknowledge the financial support from the National Natural Science Foundation of China (Nos. 81801821, 81972058, and 51872313), and Shanghai Municipal Key Clinical Specialty (No. shslczdk06701).

Availability of data and materials

All data generated or analyzed during this study are included in this article.

Declarations

Consent for publication

All authors agree to be published.

Competing interests

The authors declare that they have no competing interests.

Author details

¹Shanghai Key Laboratory of Orthopaedic Implant, Department of Orthopaedic Surgery, Shanghai Ninth People's Hospital, Shanghai Jiao Tong University School of Medicine, Shanghai 200011, China. ²Clinical and Translational Research Center for 3D Printing Technology, Shanghai Ninth People's Hospital, Shanghai Jiao Tong University School of Medicine, Shanghai 200011, China.

³Department of Orthopedics, The Second Affiliated Hospital of Harbin Medical University, Harbin 150081, China. ⁴Shanghai Electrochemical Energy Devices Research Center, School of Chemistry and Chemical Engineering and State Key Laboratory of Metal Matrix Composites, Shanghai Jiao Tong University, Shanghai 200240, China. ⁵Key Laboratory of Inorganic Coating Materials, Shanghai Institute of Ceramics, Chinese Academy of Sciences, Shanghai 200050, China.

Received: 24 January 2022 Accepted: 29 March 2022

Published online: 20 April 2022

References

- Levy SB, Marshall B. Antibacterial resistance worldwide: causes, challenges and responses. *Nat Med*. 2004;10:S122–9.
- Wang CY, Makvandi P, Zare EN, Tay FR, Niu LN. Advances in antimicrobial organic and inorganic nanocompounds in biomedicine. *Adv Ther*. 2020;3:2000024.
- Jiao Y, Niu LN, Ma S, Li J, Tay FR, Chen JH. Quaternary ammonium-based biomedical materials: state-of-the-art, toxicological aspects and antimicrobial resistance. *Prog Polym Sci*. 2017;71:53–90.
- Ding XK, Duan S, Ding XJ, Liu RH, Xu FJ. Versatile antibacterial materials: an emerging arsenal for combatting bacterial pathogens. *Adv Funct Mater*. 2018;28:1802140.
- Li X, Bai HT, Yang YC, Yoon J, Wang S, Zhang X. Supramolecular anti-bacterial materials for combatting antibiotic resistance. *Adv Mater*. 2019;31:1805092.
- Hu XL, Shang Y, Yan KC, Sedgwick AC, Gan HQ, Chen GR, He XP, James TD, Chen DJ. Low-dimensional nanomaterials for antibacterial applications. *J Mater Chem B*. 2021;9:3640–61.
- You JH, Guo YZ, Guo R, Liu XW. A review of visible light-active photocatalysts for water disinfection: features and prospects. *Chem Eng J*. 2019;373:624–41.
- Zhou ZL, Li B, Liu XM, Li ZY, Zhu SL, Liang YQ, Cui ZD, Wu SL. Recent progress in photocatalytic antibacterial. *ACS Appl Bio Mater*. 2021;4:3909–36.
- Mao CY, Xiang YM, Liu XM, Cui ZD, Yang XJ, Yeung KWK, Pan HB, Wang XB, Chu PK, Wu SL. Photo-inspired antibacterial activity and wound healing acceleration by hydrogel embedded with Ag/Ag@AgCl/ZnO nanostructures. *ACS Nano*. 2017;11:9010–21.
- Han DL, Li Y, Liu XM, Yeung KWK, Zheng YF, Cui ZD, Liang YQ, Li ZY, Zhu SL, Wang XB, Wu SL. Phototherapy-strengthened photocatalytic activity of polydopamine-modified metal-organic frameworks for rapid therapy of bacteria-infected wounds. *J Mater Sci Technol*. 2021;62:83–95.
- Wang WJ, Li GY, Xia DH, An TC, Zhao HJ, Wong PK. Photocatalytic nanomaterials for solar-driven bacterial inactivation: recent progress and challenges. *Environ Sci Nano*. 2017;4:782–99.
- Li Y, Liu XM, Tan L, Cui ZD, Yang XJ, Zheng YF, Yeung KWK, Chu PK, Wu SL. Rapid sterilization and accelerated wound healing using Zn²⁺ and graphene oxide modified g-C₃N₄ under dual light irradiation. *Adv Funct Mater*. 2018;28:1800299.
- Zhang Y, Sun PP, Zhang L, Wang ZZ, Wang FM, Dong K, Liu Z, Ren JS, Qu XG. Silver-infused porphyrinic metal-organic framework: surface-adaptive, on-demand nanoplatform for synergistic bacteria killing and wound disinfection. *Adv Funct Mater*. 2019;29:1808594.
- Mao CY, Xiang YM, Liu XM, Cui ZD, Yang XJ, Li ZY, Zhu SL, Zheng YF, Yeung KWK, Wu SL. Repeatable photodynamic therapy with triggered signaling pathways of fibroblast cell proliferation and differentiation to promote bacteria-accompanied wound healing. *ACS Nano*. 2018;12:1747–59.
- Xiang YM, Zhou QL, Li ZY, Cui ZD, Liu XM, Liang YQ, Zhu SL, Zheng YF, Yeung KWK, Wu SL. A Z-scheme heterojunction of ZnO/C₃N₄ for strengthened photoresponsive bacteria-killing and acceleration of wound healing. *J Mater Sci Technol*. 2020;57:1–11.
- Lambeth JD. Nox enzymes and the biology of reactive oxygen. *Nat Rev Immunol*. 2004;4:181–9.
- Ren YW, Liu HP, Liu XM, Zheng YF, Li ZY, Li CY, Yeung KWK, Zhu SL, Liang YQ, Cui ZD, Wu SL. Photosensitive materials for antibacterial applications. *Cell Rep Phys Sci*. 2020;1: 100245.
- Yang R, Song G, Wang L, Yang Z, Zhang J, Zhang X, Wang S, Ding L, Ren N, Wang A, Yu X. Full solar-spectrum-driven antibacterial therapy over hierarchical Sn₃O₄/PDINH with enhanced photocatalytic activity. *Small*. 2021;17:2102744.
- Makabenta JMV, Nabawy A, Li CH, Schmidt-Malan S, Patel R, Rotello VM. Nanomaterial-based therapeutics for antibiotic-resistant bacterial infections. *Nat Rev Microbiol*. 2021;19:23–36.
- Tan L, Li J, Liu XM, Cui ZD, Yang XJ, Zhu SL, Li ZY, Yuan XB, Zheng YF, Yeung KWK, Pan HB, Wang XB, Wu SL. Rapid biofilm eradication on bone implants using red phosphorus and near-infrared light. *Adv Mater*. 2018;30:1801808.
- Reddy VRM, Pallavolu MR, Gudetti PR, Gedi S, Reddy KKBY, Pejjai B, Kim WK, Kotte TRR, Park C. Review on Cu₂SnS₃, Cu₃SnS₄, and Cu₄SnS₄ thin films and their photovoltaic performance. *J Ind Eng Chem*. 2019;76:39–74.
- Munoz-Batista MJ, Fontelles-Carceller O, Ferrer M, Fernandez-Garcia M, Kubacka A. Disinfection capability of Ag/g-C₃N₄ composite photocatalysts under UV and visible light illumination. *Appl Catal B Environ*. 2016;183:86–95.
- Han QY, Lau JW, Do HC, Zhang ZJ, Xing BG. Near-infrared light brightens bacterial disinfection: recent progress and perspectives. *ACS Appl Bio Mater*. 2021;4:4397–61.
- Wang X, Shi Q, Zha Z, Zhu D, Zheng L, Shi L, Wei X, Lian L, Wu K, Cheng L. Copper single-atom catalysts with photothermal performance and enhanced nanzyme activity for bacteria-infected wound therapy. *Bioact Mater*. 2021;6:4389–401.
- Tang H, Qu X, Zhang W, Chen X, Zhang S, Xu Y, Yang H, Wang Y, Yang J, Yuan WE, Yue B. Photosensitizer nanodot eliciting immunogenicity for photo-immunologic therapy of postoperative methicillin-resistant staphylococcus aureus infection and secondary recurrence. *Adv Mater Adv Mater*. 2022;34:2107300.
- Huang B, Tan L, Liu XM, Li J, Wu SL. A facile fabrication of novel stuff with antibacterial property and osteogenic promotion utilizing red phosphorus and near-infrared light. *Bioact Mater*. 2019;4:17–21.
- Borkow G. Using copper to improve the well-being of the skin. *Curr Chem Biol*. 2014;8:89–102.
- Lokhande AC, Shelke A, Babar PT, Kim J, Lee DJ, Kim IC, Lokhandee CD, Kim JH. Novel antibacterial application of photovoltaic Cu₂SnS₃ (CTS) nanoparticles. *RSC Adv*. 2017;7:33737–44.
- Ali N, Tsega TT, Cao YC, Abbas S, Li WJ, Iqbal A, Fazal H, Xin ZL, Zai JT, Qian XF. Copper vacancy activated plasmonic Cu_{3-x}SnS₄ for highly

- efficient photocatalytic hydrogen generation: broad solar absorption, efficient charge separation and decreased HER overpotential. *Nano Res.* 2021;14:3358–64.
30. Chen FK, Zai JT, Xu M, Qian XF. 3D-hierarchical Cu₃SnS₄ flowerlike microspheres: controlled synthesis, formation mechanism and photocatalytic activity for H₂ evolution from water. *J Mater Chem A.* 2013;1:4316–23.
 31. Hu HM, Liu ZP, Yang BJ, Chen XY, Qian YT. Template-mediated growth of Cu₃SnS₄ nanoshell tubes. *J Cryst Growth.* 2005;284:226–34.
 32. Xiong YJ, Xie Y, Du GA, Su HL. From 2D framework to quasi-1D nanomaterial: preparation, characterization, and formation mechanism of Cu₃SnS₄ nanorods. *Inorg Chem.* 2002;41:2953–9.
 33. Han DL, Li Y, Liu XM, Li B, Han Y, Zheng YF, Yeung KWK, Li CY, Cui ZD, Liang YQ, Li ZY, Zhu SL, Wang XB, Wu SL. Rapid bacteria trapping and killing of metal-organic frameworks strengthened photo-responsive hydrogel for rapid tissue repair of bacterial infected wounds. *Chem Eng J.* 2020;396: 125194.
 34. Fu LH, Wan YL, Qi C, He J, Li CY, Yang C, Xu H, Lin J, Huang P. Nanocatalytic theranostics with glutathione depletion and enhanced reactive oxygen species generation for efficient cancer therapy. *Adv Mater.* 2021;33:2006892.
 35. Zhou XR, Zhu Y, Niu QY, Zeng GM, Lai C, Liu SY, Huang DL, Qin L, Liu XG, Li BS, Yi H, Fu YK, Li L, Zhang MM, Zhou CY, Liu JH. New notion of biochar: a review on the mechanism of biochar applications in advanced oxidation processes. *Chem Eng J.* 2021;416: 129027.
 36. Zhou L, Song W, Chen ZQ, Yin GC. Degradation of organic pollutants in wastewater by bicarbonate-activated hydrogen peroxide with a supported cobalt catalyst. *Environ Sci Technol.* 2013;47:3833–9.
 37. Ge L, Chen JW, Lin J, Cai XY. Light-source-dependent effects of main water constituents on photodegradation of phenicol antibiotics: Mechanism and kinetics. *Environ Sci Technol.* 2009;43:3101–7.
 38. Khan A, Zhang KK, Taraqqi-A-Kamal A, Wang XG, Chen Y, Zhang YR. Degradation of antibiotics in aqueous media using manganese nanocatalyst-activated peroxymonosulfate. *J Colloid Interf Sci.* 2021;599:805–18.
 39. Yin MC, Li ZS, Kou JH, Zou ZG. Mechanism investigation of visible light-induced degradation in a heterogeneous TiO₂/Eosin Y/Rhodamine B system. *Environ Sci Technol.* 2009;43:8361–6.
 40. Wang LW, Zhang X, Yu X, Gao EN, Shen ZY, Zhang XL, Ge SG, Liu J, Gu ZJ, Chen CY. An all-organic semiconductor C₃N₄/PDINH heterostructure with advanced antibacterial photocatalytic therapy activity. *Adv Mater.* 2019;31:1901965.
 41. Li YW, Ling WD, Han QF, Kim TW, Shi WZ. Localized surface plasmon resonances and its related defects in orthorhombic Cu₃SnS₄ nanocrystals. *J Alloy Compd.* 2015;633:347–52.
 42. Zhang X, Zhang G, Chai M, Yao X, Chen W, Chu PK. Synergistic antibacterial activity of physical-chemical multi-mechanism by TiO₂ nanorod arrays for safe biofilm eradication on implant. *Bioact Mater.* 2021;6:12–25.
 43. Guillamat-Prats R. The role of MSC in wound healing, scarring and regeneration. *Cells.* 2021;10:1729.
 44. Dong CH, Feng W, Xu WW, Yu LD, Xiang H, Chen Y, Zhou JQ. The coppery age: copper (Cu)-involved nanotheranostics. *Adv Sci.* 2020;7:2001549.
 45. Xiao JS, Chen SY, Yi J, Zhang HF, Ameer GA. A cooperative copper metal-organic framework-hydrogel system improves wound healing in diabetes. *Adv Funct Mater.* 2017;27:1604872.
 46. Rucker RB, Kosonen T, Clegg MS, Mitchell AE, Rucker BR, Uru-Hare JY, Keen CL. Copper, lysyl oxidase, and extracellular matrix protein cross-linking. *Am J Clin Nutr.* 1998;67:996s–1002s.
 47. Li Y, Fu R, Duan Z, Zhu C, Fan D. Construction of multifunctional hydrogel based on the tannic acid-metal coating decorated MoS₂ dual nanzyme for bacteria-infected wound healing. *Bioact Mater.* 2022;9:461–74.
 48. Valarmathi MT, Davis JM, Yost MJ, Goodwin RL, Potts JD. A three-dimensional model of vasculogenesis. *Biomaterials.* 2009;30:1098–112.
 49. Fan W, Crawford R, Xiao Y. Enhancing in vivo vascularized bone formation by cobalt chloride-treated bone marrow stromal cells in a tissue engineered periosteum model. *Biomaterials.* 2010;31:3580–9.
 50. Ahluwalia A, Tarnawski AS. Critical role of hypoxia sensor - HIF-1α in VEGF gene activation. Implications for angiogenesis and tissue injury healing. *Curr Med Chem.* 2012;19:90–7.
 51. Heun Y, Pogoda K, Anton M, Pircher J, Pfeifer A, Woernle M, Ribeiro A, Kameritsch P, Mykhaylyk O, Plank C, Kroetz F, Pohl U, Mannell H. HIF-1α dependent wound healing angiogenesis in vivo can be controlled by site-specific lentiviral magnetic targeting of SHP-2. *Mol Ther.* 2017;25:1616–27.
 52. Perez-Jimenez AI, Lyu D, Lu ZX, Liu GK, Ren RB. Surface-enhanced Raman spectroscopy: benefits, trade-offs and future developments. *Chem Sci.* 2020;11:4563–77.
 53. Zhou X, Hu ZW, Yang DT, Xie SX, Jiang ZJ, Niessner R, Haisch C, Zhou HB, Sun PH. Bacteria detection: from powerful SERS to its advanced compatible techniques. *Adv Sci.* 2020;7:2001739.
 54. Xu J, Liu N, Wu D, Gao Z, Song YY, Schmuki P. Upconversion nanoparticle-assisted payload delivery from TiO₂ under near-infrared light irradiation for bacterial inactivation. *ACS Nano.* 2020;14:337–46.
 55. Qiu Y, Lin M, Chen G, Fan C, Li M, Gu X, Cong S, Zhao Z, Fu L, Fang X, Xiao Z. Photodegradable CuS SERS probes for intraoperative residual tumor detection, ablation, and self-clearance. *ACS Appl Mater Inter.* 2019;11:23436–44.
 56. He J, Qiao Y, Zhang H, Zhao J, Li W, Xie T, Zhong D, Wei Q, Hua S, Yu Y, Yao K, Santos HA, Zhou M. Gold-silver nanoshells promote wound healing from drug-resistant bacteria infection and enable monitoring via surface-enhanced Raman scattering imaging. *Biomaterials.* 2020;234: 119763.
 57. Hsu YK, Chen ZB, Lin YC, Chen YC, Chen SY, Lin YG. Room-temperature fabrication of Cu nanobrushes as an effective surface-enhanced Raman scattering substrate. *CrystEngComm.* 2016;18:8284–90.

Publisher's Note

Springer Nature remains neutral with regard to jurisdictional claims in published maps and institutional affiliations.

Ready to submit your research? Choose BMC and benefit from:

- fast, convenient online submission
- thorough peer review by experienced researchers in your field
- rapid publication on acceptance
- support for research data, including large and complex data types
- gold Open Access which fosters wider collaboration and increased citations
- maximum visibility for your research: over 100M website views per year

At BMC, research is always in progress.

Learn more biomedcentral.com/submissions

